Hydrothermal Dolomites in the Early Albian (Cretaceous) Platform Carbonates (NW Spain): Nature and Origin of Dolomites and Dolomitising Fluids.

Mumtaz Muhammad Shah, Fati H. Nader, David Garcia, Rudy Swennen, Rob Ellam

Oil & Gas Science and Technology – Rev. IFP Energies nouvelles, Vol. 67 (2012), No. 1, pp. 97-122

DOI: 10.2516/ogst/2011174

Dossier

Diagenesis - Fluid-Rocks Interactions
Diagenèse minérale - Équilibres fluides-roches

Hydrothermal Dolomites in the Early Albian (Cretaceous) Platform Carbonates (NW Spain): Nature and Origin of Dolomites and Dolomitising Fluids

M.M. Shah[1-3]*, F. H. Nader[1], D. Garcia[2], R. Swennen[3] and R. Ellam[4]

1 IFP Energies nouvelles, 1-4 avenue de Bois-Préau, 92852 Rueil-Malmaison Cedex - France
2 Centre SPIN – ENSMSE, Département GENERIC, 158 cours Fauriel, 42023 Saint-Étienne - France
3 Department of Earth and Environmental Sciences, K. U. Leuven, Celestijnenlaan 200E, 3001 Heverlee - Belgium
4 Scottish Universities Environmental Research Centre, Rankine Avenue, East Kilbride, G75 0QF - United Kindom
e-mail: mumtaz-muhammad.shah@ifpen.fr - fadi-henri.nader@ifpen.fr - garcia@emse.fr
rudy.swennen@ees.kuleuven.be - rob.ellam@glasgow.ac.uk

* Corresponding author

Résumé — Dolomies hydrothermales présentes dans les carbonates de la plate-forme albienne précoce (Crétacé ; NO de l'Espagne) : nature et origine des dolomies et des fluides dolomitisants — La présente étude décrit les variations temporelle et spatiale des signatures pétrographiques et géochimiques des corps dolomitiques liés aux failles dans les régions de Ranero et El-Moro (vallée de Karrantza, montagnes cantabriques ; NO de l'Espagne). Ces corps dolomitiques se trouvent dans les carbonates albiens, déposés dans le bassin Basque-Cantabrique suite à une subsidence intense liée au rift comportant un système de failles associé suivant des orientations diverses. Des circulations de fluides ont généré des dolomies de remplacement et de cimentation, paragénétiquement suivies de divers ciments calcitiques. Des travaux de pétrographie, minéralogie et géochimie (DRX, ICP, XRF, isotopes stables de O/C et du Sr) ont aidé à distinguer les étapes hydrothermales. Deux faciès majeurs de dolomies ont été observés selon leur teneur en Fe. Les dolomies précoces sont ferrifères et remplacent le calcaire de façon plus significative que les dolomies non-ferrifères tardives. Les dolomies sont généralement stœchiométriques (de 49,76 à 51,59 % en moles de $CaCO_3$) et présentent une large plage de valeurs de $\delta^{18}O$ (de –18,7 à –10,5 ‰ V-PDB), ce qui pourrait indiquer une dolomitisation à phases multiples et/ou des degrés différents de recristallisation. Les valeurs de $\delta^{18}O$ décroissantes se trouvent en corrélation avec la diminution de la teneur en Fe dans les dolomies. Dans la région de Ranero, les dolomies présentent des valeurs de $\delta^{13}C$ légèrement moins réduites (de –0,15 à + 2,13 ‰ V-PDB) que la signature de $\delta^{13}C$ du calcaire hôte, tandis que ces valeurs sont nettement plus réduites dans la région de El-Moro (jusqu'à –2,18 ‰ V-PDB). Les calcites hydrothermales antérieures à la dolomitisation présentent des valeurs de $\delta^{18}O$ moins réduites (de –14,15 à –12,1 ‰ V-PDB) que la calcite post-dolomitisation (–18,1 ‰ V-PDB). Les données isotopiques du Sr suggèrent une interaction entre les fluides et les lithologies silicoclastiques (grès, schiste). La texture dolomitique est altérée de façon variable par la dédolomitisation et la déformation cataclastique. La dolomitisation s'est produite en au moins deux épisodes principaux. Un premier épisode de dolomitisation envahissante ferrifère résulte probablement d'une déshydratation de compactage des fluides du bassin de la dépression Basque proche et de l'écoulement de fluide hydrodynamique le long des failles/fractures dans la plate-forme de carbonates albienne. Par la suite, un second épisode de dolomitisation très chaude et locale peut être relié à l'activité magmatique et au flux de convection.

Abstract — Hydrothermal Dolomites in the Early Albian (Cretaceous) Platform Carbonates (NW Spain): Nature and Origin of Dolomites and Dolomitising Fluids — *This study documents the temporal and lateral variation in petrographic and geochemical signatures of fault-related dolomite bodies in the Ranero and El-Moro areas (Karrantza valley, Cantabrian mountains; NW Spain). These dolomite bodies are hosted in Albian carbonates, which were deposited in the Basque-Cantabrian Basin as a result of an intense rift-related subsidence with associated faulting along various orientations. Fluid circulations generated replacive and cement dolomites, paragenetically followed by various calcite cements. Petrography, mineralogical and geochemical investigations (XRD, ICP, XRF, stable and Sr isotopes) helped in distinguishing hydrothermal stages. Two major dolomite facies were observed according to their Fe-content. Early dolomites are ferroan and replace limestone more significantly than the later, non ferroan dolomites. Dolomites are generally stoichiometric (49.76 to 51.59 M% $CaCO_3$) and exhibit a broad range of depleted $\delta^{18}O$ values (–18.7 to –10.5‰ V-PDB), which may indicate multiphase dolomitisation and/or different degrees of recrystallisation. Decreasing $\delta^{18}O$ values correlate with decreasing Fe content in dolomites. In the Ranero area, dolomites show less slightly depleted $\delta^{13}C$ values (–0.15 to +2.13‰ V-PDB) relative to the host limestone $\delta^{13}C$ signature, while these values are substantially more depleted in El-Moro area (down to –2.18‰ V-PDB). Hydrothermal calcites predating dolomitisation show less depleted $\delta^{18}O$ values (–14.15 to –12.1‰ V-PDB) than post-dolomitisation calcite (–18.1‰ V-PDB). Sr isotope data suggest that the fluids interacted with siliciclastic lithologies (sandstone, shale). The dolomite fabric is variably altered through dedolomitisation and cataclastic deformation. Dolomitisation occurred in at least two main episodes. A first episode of pervasive ferroan dolomitisation probably resulted from compactional dewatering of basinal fluids from the nearby Basque trough and hydrodynamic fluid flow along the faults/fractures in the Albian carbonate platform. Subsequently, a second episode of very hot and localised dolomitisation may be related to igneous activity and convective flow.*

INTRODUCTION

Pervasive dolomitisation has been linked with various processes in diverse geological settings (Warren, 2000; Machel, 2004). Presently, various models have been proposed by a large number of workers (Adams and Rhodes, 1960; Badiozamani, 1973; Machel and Mountjoy, 1987; Cervato, 1990; Braithwaite *et al*., 2004, Nader *et al*., 2004, 2007; Zhao *et al*., 2005; Davies and Smith, 2006). Dolomite related to faults and/or fractures indicate tectonic control on the dolomitisation process but dolomite distribution also depends on the nature of host rock.

Recent integrated studies suggest that hydrothermal dolomite exists in many forms and likely to be far more common than previously thought (Berger and Davies, 1999; Moore, 2001; Cantrell *et al*., 2004; Nader and Swennen, 2004; Davies and Smith, 2006; Nader *et al*., 2009; Lopéz-Horgue *et al*., 2010; Ronchi *et al*., 2010; Conliffe *et al*., 2010). Besides a few cases of stratiform hydrothermal dolomites, these usually occur as fabric destructive, strata-discordant cutting across host limestone and concentrated along major faults (Wilson *et al*., 1990; Nader *et al*., 2004; Gasparrini *et al*., 2006; Lopéz-Horgue *et al*., 2010; Shah *et al*., 2010; Swennen *et al*., in press). Some of the known oil (Ghawar, Saudi Arabia; Cantrell *et al*., 2004) and gas (North field, Arabian Gulf; Sudrie *et al*., 2006) carbonate reservoirs consist of porous dolomites, which are probably partly hydrothermal in origin. It is important to understand this particular dolomitisation process, which may be of major economic importance.

The present study concerns momentous dolomite exposures in early Albian (Cretaceous) platform carbonates in Northwest Spain. It aims at deciphering the mechanism and extent of dolomitisation and their relationship to the regional tectonic scenario, and to determine the nature and origin of the dolomitising fluids. Such aspects were not substantially discussed yet. For this purpose, petrographic and geochemical studies were carried out in two sites (Ranero and El-Moro, north western Spain). Hence, additional understanding of the exposed dolomites in the study area and their dolomitising fluids is presented in this paper.

1 LOCATION AND GEOLOGICAL SETTINGS

The study area is part of the Basque Cantabrian Basin (BCB), which hosts the only onshore Ayoluengo oil field discovered in north-western Spain (Abeger *et al*., 2005). The study area is bounded by Basque and Asturian massifs in the east and west, while the Bay of Biscay and Tertiary Ebro/Duero basins mark the northern and southern boundaries respectively *(Fig. 1a)*. The studied sites, Ranero and El-Moro areas are located at the border of Basque country and province of Cantabria (NW Spain), near the town of Ramales *(Fig. 1b)*.

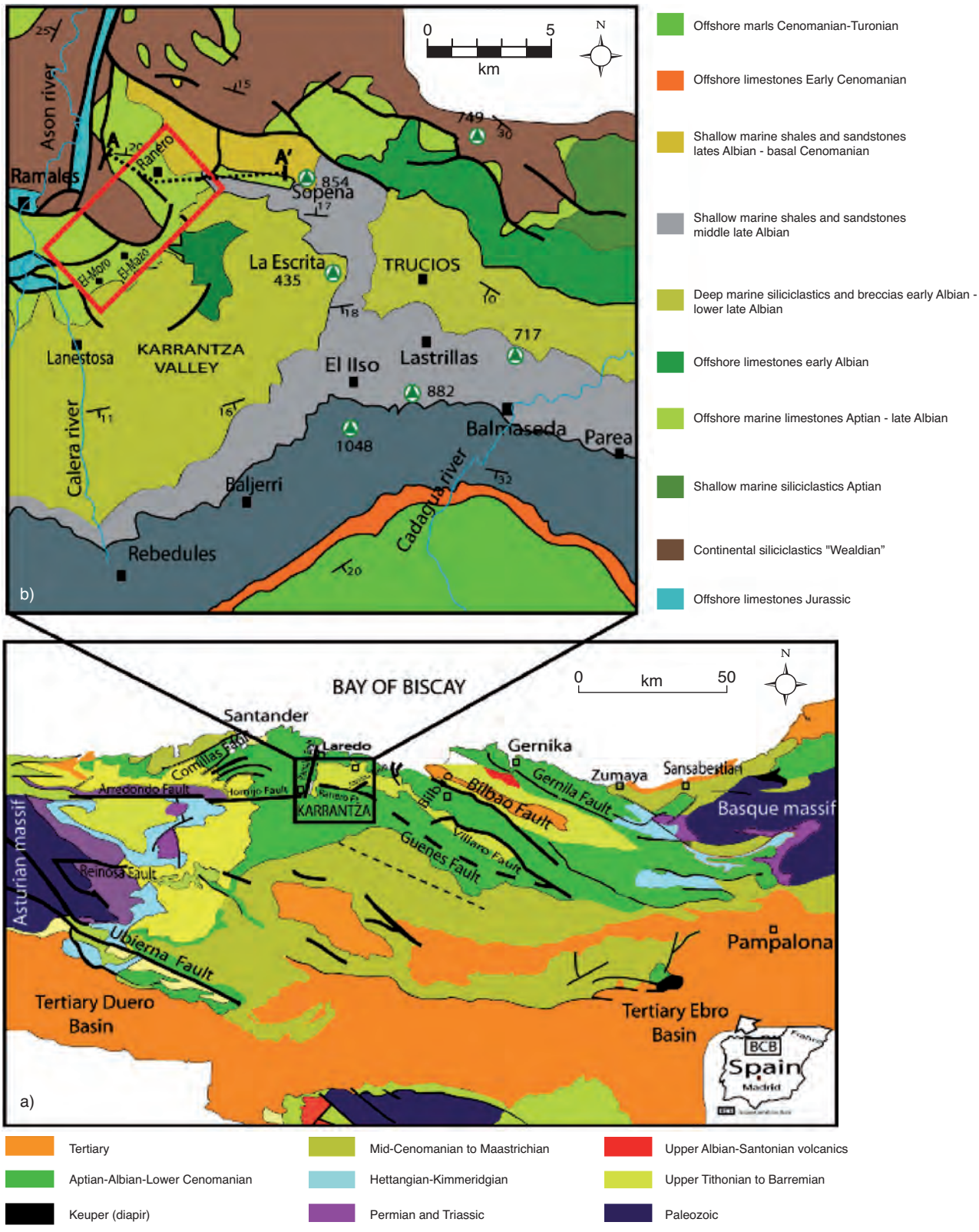

Figure 1

a) Tectono-stratigraphic map of the Basque-Cantabrian basin, showing Tertiary to Paleozoic rocks and major faults. b) Detailed stratigraphic succession and faults surrounding the study area (red rectangle showing Ranero, El-Moro and El-Mazo areas; modified from Gibbons and Moreno, 2002 and Lopez-Horgue *et al*., 2009).

1.1 Tectonic Evolution

In the BCB, two periods of fault-controlled regional subsidence (from middle Triassic to middle Jurassic and early to late Cretaceous) occurred (Rat, 1959; Pujalte, 1977; Garcia-Mondéjar, 1989; Olivet, 1996; Lopéz-Horgue *et al*., 2010). Besides regional subsidence, three major tectonic events are reported in the BCB:

- Permo-Triassic rifting stage;
- Late Jurassic-Early Cretaceous rifting and opening of Bay of Biscay; and
- Eocene-Oligocene Pyrenean orogeny.

The BCB formed by the Late Jurassic tectonic extension between the European and Iberian plates, which resulted in the opening of the Bay of Biscay and caused the deposition of a thick Cretaceous sedimentary sequence (Boillot and Malod, 1988; Malod and Mauffret, 1990; Olivet, 1996). Later on, the Iberian plate rotated back northward and collided with the European plate during Campanian to Maastrichtian time (Gibbons and Moreno, 2002). During the Early Cretaceous rifting period, BCB underwent NNE-SSW direction of simple stretching perpendicular to the axes of the main NW-SE structural trend (Montadert *et al*., 1979; Grimaud *et al*., 1982; Boillot and Malod, 1988; Malod and Mauffret, 1990). Later on, this NNE-SSW direction of simple stretching changed to NW-SE direction as the simple extension was replaced by left lateral strike-slip motion along the main NW-SE faults as evidenced in the study area (Ranero and Güenes faults). This change in the direction is linked to the anticlock-wise rotation of the Iberian plate with respect to European plate and spreading in the western part of the Bay of Biscay (Montadert *et al*., 1979; Boillot and Malod, 1988). Trans-tensional movements along these NW-SE oriented faults produced oblique slip and pull-apart basins, where thick sediment accumulation took place.

The study area and its surroundings encompass various tectonic features, which include NW-SE oriented (Güenes and Ranero faults), N-S oriented (Ramales fault), E-W oriented (Arredondo and Hornijo faults) as well as other small scale NE-SW directed faults and fault splays, indicating the extensional history *(Fig. 1a)*. In the study area, dolomite bearing, left-lateral Ranero fault is believed to be the splay of NW-SE oriented oblique-slip Güenes fault, formed during Early-Mid Albian (Garcia-Mondéjar *et al*., 1996; Aranburu *et al*., 1994). So, these NW-SE oriented faults are related to Early Cretaceous rifting in the BCB (Grimaud *et al*., 1982; Boillot and Malod, 1988; Olivet, 1996). The N-S oriented Ramales fault is a basement rooted listric fault (García-Mondéjar and Pujalte, 1975), while the E-W oriented Arredondo and Hornijo faults (Early-Mid Albian) post-date NW-SE oriented faults and fractures (García-Mondéjar, 1985).

1.2 Lithostratigraphy

In the study area, the Aptian carbonates are mostly shallow marine, while early to mid-Albian carbonates change from shallow marine to reefal facies and show deltaic conditions (sandstones and lutites) in the upper most part (*Fig. 2*; Rosales, 1995). Four sequences bounded by unconformities occur in the Albian stage, which include early to late Albian platform to slope carbonates (basinward equivalent to marls), carbonate breccia and siliciclastic deposits *(Fig. 2, 3)* (García-Mondéjar *et al*., 2005). The Aptian-Albian carbonates in the study area mostly consist of rudist limestones accumulated in places and exhibit rapid changes of lateral facies into siliciclastic sediments, while warm and wet climatic conditions are indicated by the presence of reefal faunas, lack of evaporitic deposits, common storm deposits and frequent fossil wood in deltaic facies (García-Mondéjar, 1990; Rosales and Pérez-García, 2010). The study area mostly comprises early- to late- Albian platform to slope carbonates and shallow to deep-marine siliciclastics in the basinal regime, while dolomitisation being mostly restricted to early Albian carbonates *(Fig. 2, 3)* (Lopéz-Horgue *et al*., 2009, 2010; Rosales and Pérez-García, 2010).

Four main stratigraphic units are recognised, which include the Sopeña and Ranero in the platform region, while La Escrita (lower half of Valmaseda Formation) and Río Calera units occur in the vicinity of the deep and shallow basinal areas (Aranburu, 1998; Lopéz-Horgue, 2000; Rosales and Pérez-García, 2010). The Sopeña and Ranero units consist of shallow marine carbonates and are stratigraphically correlated with Ramales Formation in the Ramales area (Lopéz-Horgue *et al*., 2009). Towards the south, basinal marls, shales and siltstones of Río Calera unit onlap these shallow marine carbonates (Sopeña and Ranero units), unconformably overlain by shallow marine siliciclastics of La Escrita unit *(Fig. 3)*. Laterally, the Río Calera and La Escrita units can be correlated with Ranero and Sopeña units, respectively (Lopéz-Horgue *et al*., 2009; Rosales and Pérez-García, 2010). The short distance between the platform carbonates and the basinal deposits suggests the formation of an intra-platform trough rather than a deep basin (Garcia-Mondéjar, 1996). Platform to slope carbonate successions show two major carbonate depositional systems, which include early Albian aggradational steep-sloping platform and late Albian low-gradient widespread carbonate bank development separated by a regional unconformity (*Fig. 3*; Rosales and Pérez-Garcia, 2010).

During late Albian and Turoninan stage, at least 50 m sea-level fall in the study area and its surroundings resulted in development of a paleokarst system (García-Mondéjar, 1990; Lopéz-Horgue *et al*., 2010), hence formed metre-scale cavities (due to dissolution in limestone and localised in joints) that were filled by shallow marine sandstones (García-Mondéjar, 1990). Besides the development of paleokarst

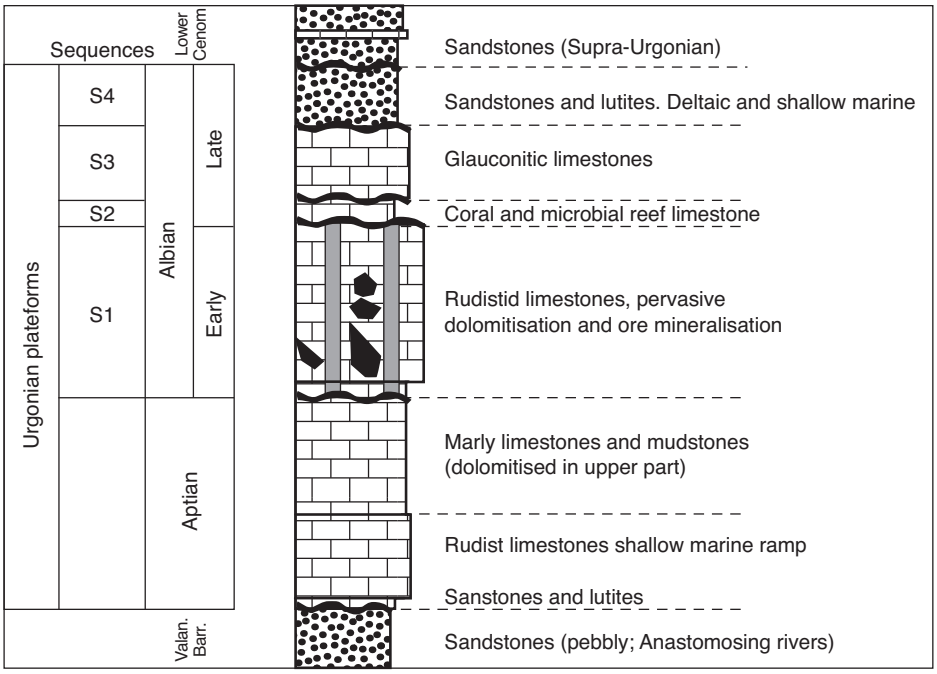

Figure 2

Stratigraphic column for the Ranero and its surrounding areas, northwestern Basque-Cantabrian basin, showing the main facies of four Urgonian sedimentary sequences. The ore bodies are restricted to dolomitised unit (modified from Rosales and Pérez-Garcia, 2010 and Lopéz-Horgue *et al*., 2010).

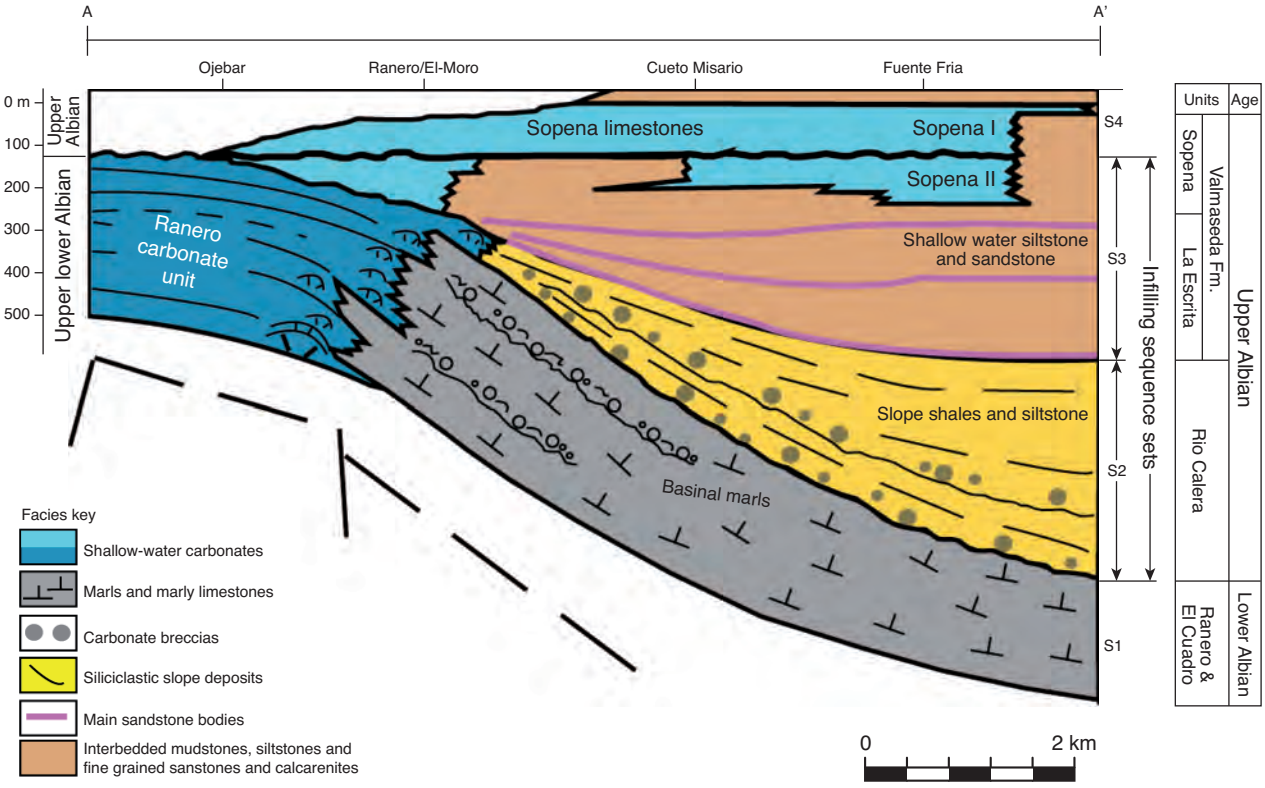

Figure 3

Stratigraphic cross-section (A-A' in *Fig. 1b*), showing unconformities and lateral variations from platform to basinal facies in the study area and its surroundings (modified from Rosales and Pérez-Garcia, 2010).

system, hydrothermal karstification is also observed in the study area. These two karst systems show distinct characteristic features, which helped in their recognition (Bosák, 1998; Aranburu *et al*., 2002; Swennen *et al*., in press).

2 METHODS

Aerial photographs helped in delineating brown to dark-grey colored dolomite bodies in the light grey colored host limestone *(Fig. 4)*. Systematic sampling was carried out across the dolomite bodies. Each sample represented certain dolomite facies and/or host limestone in the Ranero and El-Moro areas *(Fig. 4)*. Rock slabs and thin sections were stained with Alizarin Red S and potassium ferricyanide (Dickson, 1966) to differentiate ferroan/non-ferroan dolomite and calcite. Petrographic studies were carried out using conventional (Nikon ECLIPSE LV 100 POL) and cathodoluminescence microscopy (Cathodyne OPEA; operating conditions were 12 to 17 kV gun potential, 350 to 600 μA beam current, 0.05 Torr vacuum) of 260 thin sections. 54 selected samples were analysed (to determine bulk mineralogy, stoichiometry and crystal ordering of the different dolomite phases) using a PANalytical X'Pert PRO X-ray diffractometer (Cu-Kα radiation ~ 45 kV, 40 mA). The scan speed was set at 0.2°θ min^{-1} and sampling interval at 0.001°θ per step. The dolomite stoichiometry was determined by applying Lumsden's equation (1979) to the measured d104 spacing (M = 333.3 × d-spacing – 911.99) and expressed as mol% $CaCO_3$.

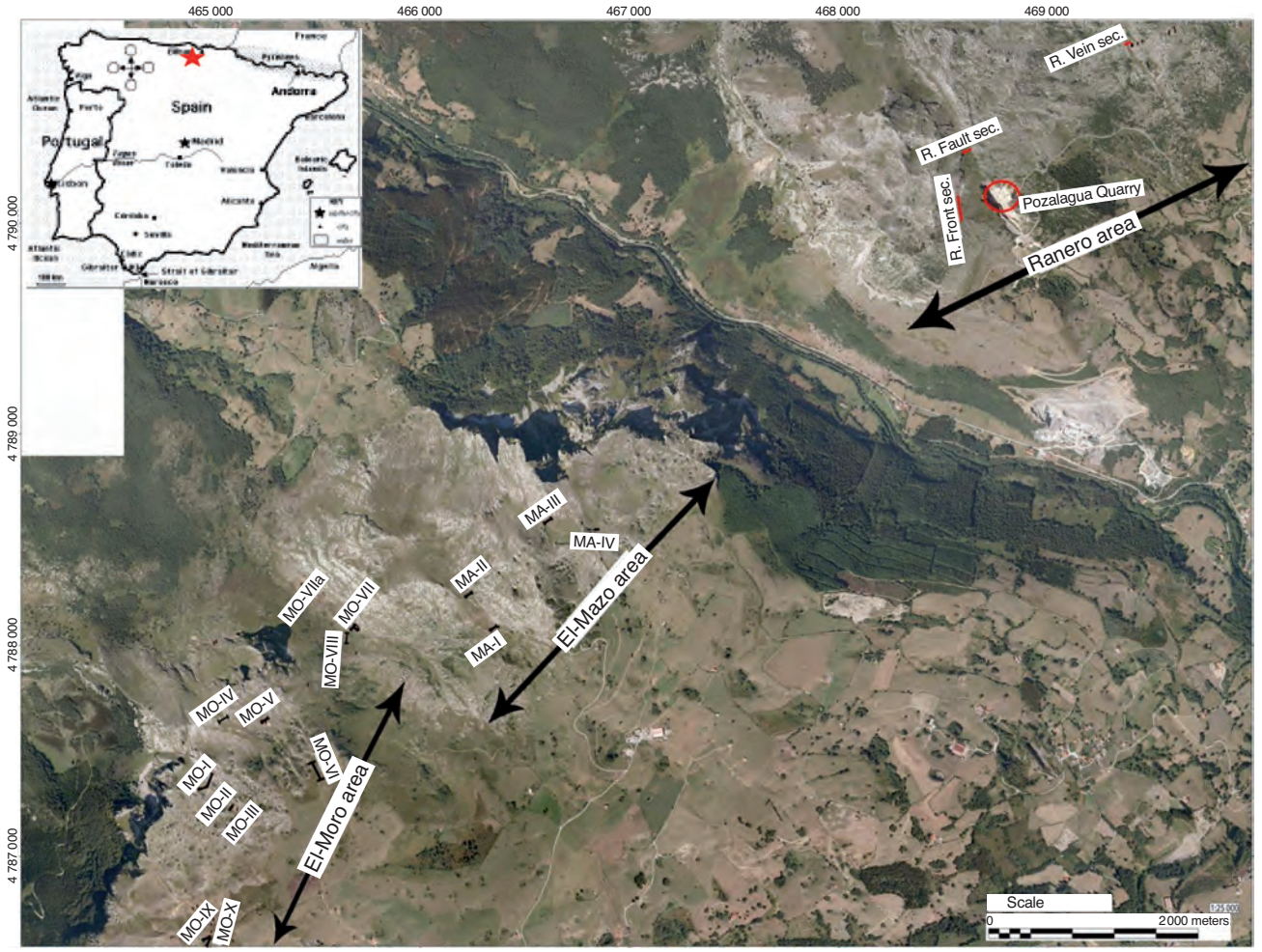

Figure 4

Aerial photograph showing the location of the sampled sections in the Ranero, El-Moro and El-Mazo areas, while inset shows the geographic location of the study area (red star).

Geochemical analyses of the selective rock phases and whole rock samples were obtained by means of X-Ray Fluorescence (XRF) and Inductively-Coupled Plasma Optical Emission Spectrometry (ICP-OES) depending on the amount of material available from micro-drillings and/or plugs. In total 250 samples were analysed by ICP-OES, and 128 samples by XRF in École des Mines, Saint-Étienne. XRF analysis was performed with a SRS3400 spectrometer, using glass discs/pressed pellets for major/trace elements, respectively. ICP-OES analysis is performed on a JI Activa sequential device using acid solutions prepared by HF digestion. Both analytical routines are calibrated against geostandards. Coupling these techniques is effective in overcoming the main drawback of each one, *i.e.* sensitivity for minor and trace elements by XRF (below 0.1% and 10 ppm) and reproducibility by ICP-OES (5%).

Stable isotope analyses ($\delta^{18}O$ and $\delta^{13}C$) of 275 selected samples of different dolomite types, calcite cement and host limestone were carried out in the Department of Geology, University of Erlangen, Germany and Département Géologie, Jean Monnet Université, Saint-Étienne *(Tab. 1)*. All stable isotope values are reported in per mil (‰) relative to Vienna Pee Dee Belemnite (V-PDB) by assigning a $\delta^{13}C$ value of + 1.95‰ and a $\delta^{18}O$ value of – 2.20‰ to NBS19. The carbonate powders were reacted with 100% phosphoric acid (density > 1.9; Wachter and Hayes, 1985) at 75°C in an online carbonate preparation line (Carbo-Kiel – single sample acid bath) connected to a Finnigan Mat 252 mass-spectrometer. Dolomite isotopic composition values are corrected by fractionation factors given by Rosenbaum and Sheppard (1986). Based on replicate analysis of laboratory standards, reproducibility is better than ± 0.02‰ for $\delta^{13}C$ and ± 0.03‰ for $\delta^{18}O$.

Fifteen Sr isotope analyses of the selected dolomite samples were performed at the Scottish Universities Environmental Research Centre in Glasgow. These analyses are used to reveal radiogenic influence that may have changed the original Sr isotope signature of the carbonates. Carbonate samples were leached in 1M ammonium acetate prior to acid digestion. Calcite was digested in 1M acetic acid, and dolomite in 6M HCl. Sr was separated in 2.5M HCl using Bio-Rad AG50W X8 200-400 mesh cation exchange resin. Total procedure blank for Sr samples prepared using this method is < 200 pg. In preparation for mass spectrometry, Sr samples were loaded onto single Ta filaments with 1N phosphoric acid. Sr samples were analysed on a VG Sector 54-30 multiple collector mass spectrometer. A ^{88}Sr intensity of 1 V (1×10^{-11} A) ± 10% was maintained and the $^{87}Sr/^{86}Sr$ ratio was corrected for mass fractionation using $^{87}Sr/^{86}Sr = 0.1194$ and an exponential law. The VG Sector 54-30 mass spectrometer was operated in the peak-jumping mode with data collected as 15 blocks of 10 ratios. For this instrument NIST SRM987 gave 0.710260 ± 11 (1 SD, n = 17) during the course of this study. The representative analytical data are given in Table 1.

TABLE I - PART I

Major and trace element geochemistry, O- and C- stable isotope, Sr- isotope and stoichiometric data from the Ranero and El-Moro areas

Site	Sample	Stage	Al_2O_3	Fe_2O_3	MnO	MgO	CaO	Zn	Ba	$\delta^{13}C$	$\delta^{18}O$	$^{87}Sr/^{86}Sr$	Stoich.
QUARRY	R515A3	CCD_II	0.06	0.03	0.012	21.52	31.85	7.4	0.70	1.12	-18.23		
QUARRY	R515A2	CCD_II	0.06	0.07	0.014	21.81	32.00	4.3	0.81	1.30	-18.22		
QUARRY	RQ35B	DS	0.76	0.30	0.013	20.90	27.24	6.7	1.30	1.05	-18.01		
QUARRY	R511E	DS	1.08	0.95	0.013	21.00	30.52	6.9	1.46	0.85	-17.83		
QUARRY	R511B	DS	0.41	0.92	0.014	21.08	31.90	4.3	1.47	0.79	-17.72		
QUARRY	RQ41A	CCD_II								1.54	-17.64		50.86
QUARRY	RQ26A	DS	1.19	0.39	0.011	18.61	30.06	40.8	1.51	1.64	-17.58		
QUARRY	RQ29HA	DS	0.58	0.26	0.012	19.93	27.99	3.7	1.80	0.47	-17.53		
QUARRY	RQ31B	ZD	0.03	0.47	0.037	20.89	29.14	4.8	0.86	1.45	-17.51		
QUARRY	RQ31A	ZD	0.33	0.18	0.013	20.00	28.80	10.1	0.99	1.18	-17.33		49.75
QUARRY	RQ29HB	CCD_II	0.02	0.07	0.016	19.53	29.40	20.8	2.25	0.64	-16.87		
QUARRY	RQ28A	CCD_II	0.02	0.12	0.011	19.90	30.18	3.5	0.51	0.98	-16.79		
QUARRY	RQ40A	DS	0.02	0.20	0.022	20.81	28.52	2.3	0.55	1.67	-16.75		
QUARRY	R524	CCD_II	0.06	0.04	0.011	20.15	29.87	8.4	1.24	0.54	-16.73		
QUARRY	RQ34A	CCD_II	0.02	0.13	0.020	20.24	28.11	2.6	0.66	1.11	-16.65		
QUARRY	R513B	CCD_II	0.06	0.05	0.014	20.30	32.32	2.4	0.70	2.02	-16.65		

TABLE I - PART II

Site	Sample	Stage	Al_2O_3	Fe_2O_3	MnO	MgO	CaO	Zn	Ba	$\delta^{13}C$	$\delta^{18}O$	$^{87}Sr/^{86}Sr$	Stoich.
QUARRY	RQ44A	ZD	0.03	0.07	0.018	20.77	29.62	7.2	33.70	0.42	-16.36		
QUARRY	R514A1	DS	0.37	1.40	0.029	18.70	32.44	8.4	2.60	0.00	-16.29		
QUARRY	R525	CCD_II	0.05	0.10	0.011	19.19	30.85	7.0	2.68	-1.71	-16.16		
QUARRY	R514A2	DS	0.23	1.16	0.033	19.57	34.40	5.9	2.21	0.16	-16.05		
QUARRY	RQ36B	CCD_I	0.03	0.48	0.029	20.09	28.84	2.2	0.48	0.82	-15.79		
QUARRY	RQ43B	CC_I								0.54	-15.54		51.00
QUARRY	RQ43C	DS	1.43	0.59	0.019	7.98	12.73	1529.1	3240	0.97	-15.24		50.37
QUARRY	RQ36A	CCD_I	0.03	0.57	0.034	19.94	28.96	3.4	2.56	0.82	-14.82		
QUARRY	RQ45A	Ba	0.01	0.00	0.004	0.23	53.87	3.7	153.1	1.34	-13.86		
QUARRY	R517B	Ba	0.12	0.09	0.013	19.71	29.77	10.2	1.77	2.76	-12.07		50.28
QUARRY	R513A2	CC_I	0.03	0.05	0.012	0.39	56.96	2.9	2.41	1.82	-12.03		
QUARRY	R513A1	CC_I	0.02	0.04	0.011	0.26	56.06	2.9	2.01	1.92	-11.61		
QUARRY	R517A	Ba	0.02	0.02	0.010	0.25	58.31	4.9	2.80	2.28	-8.97		
FAULT	RC21A	CCD_II	0.01	0.06	0.011	17.99	30.98	21.7	6.63	0.94	-17.37		50.1
FAULT	RC4A	CCD_I	0.06	0.79	0.040	20.34	32.71	4.3	3.02	0.72	-16.19		
FAULT	RC23A	LS	0.06	0.03	0.006	0.53	58.00	13.6	1.33	0.67	-15.90		
FAULT	RC7A	CCD_I	0.02	0.69	0.040	20.83	28.40	4.6	11.26	0.78	-15.45		
FAULT	RC19A	LS	0.04	0.02	0.006	0.38	57.69	2.6	2.98	1.78	-14.65		
FAULT	RC13A	CCD_I	0.01	0.68	0.041	20.10	28.34	4.0	6.15	0.45	-14.37		
FAULT	RC15A	CCD_I	0.01	1.28	0.046	14.79	38.50	4.8	5.23	0.59	-12.28		50.1
FAULT	RC18A	CC_II	0.07	0.33	0.009	0.55	56.12	7.6	4.71	1.65	-11.64		
FAULT	RC22A	CCD_I	0.06	0.06	0.017	19.64	37.64	10.0	0.67	1.70	-10.28		
FAULT	RC3A	TC	0.04	1.18	0.047	5.86	50.09	14.1	11.32	-5.03	-8.92		
FAULT	RC20	CCD_II	0.01	0.07	0.010	19.40	35.44	13.2	1.52				50.1
FAULT	RC5	CCD_I	0.02	0.94	0.044	20.35	33.35	4.7	2.30				50.1
FAULT	RC17	CCD_I	0.08	1.37	0.043	18.83	34.26	23.6	5.85				51.7
FRONT	RT999A	CCD_II	0.05	0.20	0.022	19.22	29.53	3.4	1.38	-0.91	-19.12		
FRONT	RT72A	CCD_II	0.01	0.06	0.016	18.87	30.35	5.3	1.53	0.46	-18.84		49.89
FRONT	RT74HA	CCD_II	0.01	0.06	0.013	17.04	23.17	1.8	0.75	1.14	-18.59	0.708129	50.63
FRONT	RT73A	CCD_II	0.34	0.15	0.017	20.31	29.99	4.5	1.95	0.47	-18.48		
FRONT	RT77B	CCD_II	0.02	0.14	0.025	18.61	30.28	10.2	2.39	1.27	-18.45		
FRONT	RT74HB	CCD_II	0.02	0.13	0.021	20.27	30.36	2.9	0.92	1.17	-18.19	0.708134	50.81
FRONT	RT68B	CCD_II	0.09	0.16	0.025	19.77	29.59	19.7	6.85	1.14	-17.28		
FRONT	RT66A	LS	0.14	0.06	0.009	0.67	55.23	3.5	2.20	2.35	-17.10		
FRONT	RT75A	CCD_I	0.05	0.60	0.034	17.32	38.02	4.0	6.67	-0.28	-16.32		
FRONT	RT71A	DEDOL	0.24	1.35	0.042	18.75	33.79	4.9	4.17	0.85	-14.08		
FRONT	RT78	LS	0.08	0.06	0.008	0.52	57.05	14.8	4.36	2.68	-13.18		
FRONT	RT69	CCD_I	0.10	1.26	0.061	16.50	33.45	6.7	4.78	0.73	-12.95		
FRONT	RT70B	DEDOL	0.13	2.17	0.087	15.90	35.81	3.6	8.56	-1.45	-11.31		
FRONT	RT76A	DEDOL	0.20	0.28	0.019	20.96	34.08	6.3	6.48	-3.16	-10.81		

TABLE I - PART III

Site	Sample	Stage	Al_2O_3	Fe_2O_3	MnO	MgO	CaO	Zn	Ba	$\delta^{13}C$	$\delta^{18}O$	$^{87}Sr/^{86}Sr$	Stoich.
BRECCIA	R529C	WC	0.01	0.01	0.019	0.37	53.90	1.6	3.59	0.50	-18.62		
BRECCIA	R529D	CCD_I	0.04	0.21	0.029	19.54	30.00	2.8	6.72	0.93	-15.82		49.76
BRECCIA	R530A	CCD_I	0.08	1.07	0.053	20.37	30.53	4.8	1.17	1.52	-14.47		
BRECCIA	R115A	CCD_I	0.04	1.12	0.061	19.80	30.52	3.5	2.13	1.08	-13.23		
VEIN	RV57A	CCD_II	0.03	0.15	0.020	20.57	29.47	2.7	5.85	0.87	-16.71		
VEIN	R519A	WC	0.01	0.02	0.007	0.27	51.82	2.4	20.76	-0.66	-16.09		
VEIN	RV63	CCD_I	0.03	0.74	0.044	20.44	32.30	2.5	1.02	1.4	-15.09		
VEIN	RV59A	CCD_I	0.02	1.13	0.076	21.14	31.43	7.8	1.57	1.14	-14.18	0.708473	
VEIN	RV61A	CCD_I	0.02	0.74	0.068	21.22	33.02	12.3	2.37	1.52	-14.15		
VEIN	R521B	CCD_I	0.06	0.63	0.039	20.17	32.50	3.2	1.53	1.31	-14.03		
VEIN	RV65A	ZD	0.01	0.91	0.054	19.54	28.70	2.8	4.34	0.89	-13.83		
VEIN	RV54A	CCD_I	0.01	1.10	0.053	20.51	32.70	2.3	1.66	0.81	-13.73		
VEIN	R521C	CCD_I	0.05	0.56	0.039	18.77	33.93	5.1	1.83	1.36	-13.62		
VEIN	RV55A	CCD_I	0.03	1.29	0.088	19.55	32.76	9.7	2.33	1.20	-13.56		
VEIN	RV51A	CCD_I	0.01	0.83	0.056	19.85	28.81	3.3	2.65	1.15	-13.28		
VEIN	RV58A	CCD_I	0.01	1.24	0.057	21.13	31.12	3.1	2.52	1.16	-13.09		
VEIN	R521A	CC_I	0.01	0.03	0.010	0.18	53.90	4.7	2.60	1.02	-13.09		
VEIN	RV62A	CCD_I	0.01	0.82	0.066	20.39	29.75	3.7	1.01	1.27	-12.81		
VEIN	RV64A	CC_II	0.02	0.02	0.005	0.26	56.00	9.5	1.94	1.99	-12.68		
VEIN	R522	CC_I	0.03	0.05	0.011	0.32	57.36	3.1	2.25	1.55	-11.85		
VEIN	RV49A	CC_I	0.01	0.04	0.009	0.22	56.00	6.1	1.34	1.12	-11.80	0.708443	
VEIN	R207B	CC_I	0.02	0.02	0.013	0.37	52.65	3.2	4.39	1.84	-11.28		
VEIN	RV48A	LS	0.01	0.07	0.011	0.61	54.61	1.8	1.47	1.18	-11.11		
VEIN	RV47B	LS	0.17	0.30	0.017	1.35	53.71	1.9	3.72	1.3	-10.08		
VEIN	R209A	LS	0.01	0.06	0.006	0.47	57.57	0.0	8.54	2.50	-8.39		
VEIN	R208A	LS	0.02	0.11	0.005	0.43	59.48	0.0	7.27	2.07	-7.44		
VEIN	RV60A	TC	0.01	1.33	0.067	21.40	31.23	3.1	0.87	-5.30	-6.93		
VEIN	R211aC	LS	0.02	0.12	0.006	0.39	57.62	0.0	9.87	1.93	-6.39		
MO-I	R239A	CCD_II	0.04	0.00	0.011	20.62	28.92	3.4	3.19	-2.32	-18.72		49.94
MO-I	R227A	CCD_II	0.03	0.01	0.015	18.01	31.33	295.8	8.91	-0.25	-18.49		50.12
MO-I	R231B	CCD_II	0.39	0.24	0.011	20.62	28.57	75.0	6.61	-0.91	-18.19		50.26
MO-I	R234A	CCD_II	0.03	0.02	0.012	21.16	31.52	20.6	1.28	-0.92	-17.93		49.6
MO-I	R231A	CCD_II	0.04	0.00	0.013	20.52	29.90	120.8	2.27	-1.15	-17.87	0.70815	49.98
MO-I	R239B	CCD_II	0.39	0.17	0.012	20.91	29.30	14.5	98.89	-1.39	-16.78		50.17
MO-I	R232A	CCD_II	0.03	0.01	0.011	19.44	29.38	87.8	0.75	0.85	-15.89		
MO-I	R228A	CCD_I	0.05	0.52	0.049	22.31	32.14	199.1	2.45	1.50	-14.54		
MO-I	R245A	WC	0.01	0.00	0.006	0.28	56.36	13.7	18.78	-1.06	-17.32		
MO-I	R247B	ZD	0.03	0.63	0.044	20.79	29.71	25.4	5.87	0.41	-14.98		
MO-I	R247A	ZD	0.10	0.69	0.044	21.47	29.20	39.2	4.46	0.79	-14.39		50.01
MO-I	R242C	CCD_I	0.02	1.00	0.062	20.84	28.67	68.4	1.50	1.23	-14.23		

TABLE I - PART IV

Site	Sample	Stage	Al_2O_3	Fe_2O_3	MnO	MgO	CaO	Zn	Ba	$\delta^{13}C$	$\delta^{18}O$	$^{87}Sr/^{86}Sr$	Stoich.
MO-I	R242B	CCD_I	0.01	0.84	0.058	20.53	27.81	47.8	1.21	1.28	-14.12		
MO-II	R263A	CCD_II	0.04	0.22	0.027	20.44	29.41	28.4	2.97	-0.46	-17.77		50.07
MO-II	R257A	CCD_I	0.03	0.44	0.038	19.62	28.60	74.2	9.29	-0.13	-15.43		49.99
MO-II	R263B	ZD	0.21	0.55	0.038	19.95	28.00	23.0	3.38	1.10	-15.39		
MO-II	R250C	LS	0.10	0.16	0.015	3.26	53.01	98.5	5.62	2.85	-15.16		
MO-II	R256A	ZD	0.03	0.59	0.055	21.26	29.44	120.7	2.20	1.04	-15.10		
MO-II	R256B	ZD	0.04	0.70	0.065	20.66	29.37	104.1	3.30	0.61	-14.72		
MO-II	R250B	CCD_I	0.39	0.61	0.047	16.92	35.63	382.0	10.75	0.57	-13.89		
MO-II	R268A	LS	0.08	0.03	0.004	0.61	55.37	14.3	5.88	3.55	-11.61		
MO-III	R284A	WC	0.01	0.01	0.010	0.70	51.80	5.4	1.91	0.27	-20.22		
MO-III	R283A	WC	0.01	0.01	0.010	0.31	56.37	4.7	1.23	0.89	-19.43		
MO-III	R292A	CCD_I	0.03	0.41	0.040	21.60	31.96	17.1	0.96	0.99	-15.7		
MO-III	R290B	CCD_I	0.28	0.56	0.042	21.76	28.87	34.1	9.00	0.78	-15.43		
MO-III	R270A	CCD_I	0.04	0.40	0.047	20.16	30.01	260.7	2.03	1.13	-14.90		
MO-III	R277aB	CCD_I	0.04	0.81	0.057	20.70	29.91	40.9	3.50	0.85	-14.71		
MO-III	R290A	CCD_I	0.03	0.59	0.045	21.51	30.20	25.7	0.88	0.74	-14.63		50.22
MO-III	R291A	CCD_I	0.23	0.78	0.048	21.70	30.70	47.9	38.76	1.01	-14.55		
MO-III	R272A	CCD_I	0.04	0.81	0.055	21.75	31.35	495.5	1.93	1.53	-13.75		50.56
MO-III	R270B	CCD_I	0.05	0.48	0.049	20.98	30.19	374.8	1.40	2.05	-13.57		49.82
MO-III	R277A	CCD_I	0.03	0.84	0.061	19.49	31.87	399.3	1.75	0.83	-13.38		
MO-III	R278A	CCD_I	0.05	1.76	0.072	20.46	31.76	178.3	1.95	1.49	-13.22		
MO-III	R278B	Zn	0.04	2.21	0.125	14.78	33.73	4 827.4	16.73	-1.16	-11.82		49.85
MO-IV	R304A	WC	0.01	0.00	0.004	0.27	52.21	3.2	3.25	1.10	-19.59		
MO-IV	R301A	CCD_II	0.03	0.00	0.011	19.58	28.93	25.3	85.17	-1.10	-18.59		
MO-IV	R317A	CCD_II	0.03	0.14	0.021	19.21	30.08	202.2	12.26	-0.93	-18.16	0.708265	51.13
MO-IV	R308A	WC	0.01	0.01	0.007	0.26	53.10	33.3	5.87	0.79	-17.86	0.708815	
MO-IV	R310bA	WC	0.01	0.00	0.006	0.27	56.32	14.9	4.12	0.74	-17.29		
MO-IV	R311A	CCD_I	0.02	0.04	0.076	20.91	28.54	49.7	2.71	-0.38	-15.69		49.9
MO-IV	R311B	CCD_I	0.04	0.59	0.061	22.19	27.86	170.2	32.49	0.47	-15.51		50.2
MO-IV	R304B	CCD_I	0.05	1.38	0.058	17.00	30.85	133.0	9.45	2.45	-12.85		
MO-IV	R312PA	Zn	0.07	1.85	0.082	10.44	46.17	3 123.9	13.57	-3.2	-11.45		
MO-IV	R309aC	Zn	0.03	1.31	0.058	10.77	39.01	1 688.9	20.76	-2.77	-10.35		
MO-IV	R310bB	Zn	0.06	1.62	0.076	4.13	49.73	7 071.6	5.53	-5.58	-7.43		
MO-IV	R312PB	Zn	2.84	1.55	0.035	7.26	42.85	3 201.3	12.14	-3.94	-7.23		
MO-IV	R300D	CCD_II	0.05	0.03	0.012	18.41	29.31	68.6	0.60				49.76
MO-IX	R376A	CCD_II	0.05	0.04	0.027	22.20	30.97	92.6	1.59	-2.67	-17.47		
MO-IX	R500A	ZD	0.27	1.05	0.053	19.56	30.74	336.1	5.65	0.76	-16.72		
MO-IX	R369A	CCD_I	0.06	0.53	0.043	21.72	30.85	972.0	4.71	-0.59	-16.18		
MO-IX	R373B	DS	0.98	0.71	0.050	20.76	30.12	3 833.4	12.94	-0.21	-15.9		
MO-IX	R372A	DS	0.46	0.71	0.033	21.28	30.80	9 568.2	8.88	0.27	-15.69		

TABLE I - PART V

Site	Sample	Stage	Al_2O_3	Fe_2O_3	MnO	MgO	CaO	Zn	Ba	$\delta^{13}C$	$\delta^{18}O$	$^{87}Sr/^{86}Sr$	Stoich.
MO-IX	R500B	ZD	0.26	1.02	0.048	19.09	30.56	452.9	4.64	1.41	-15.29		
MO-IX	R371xC	CCD_I	0.03	0.53	0.059	20.78	30.35	7 160.6	2.16	0.6	-15.29		
MO-IX	R373A	CCD_I	0.03	0.30	0.048	21.94	30.75	201.1	0.82	0.91	-15.26		
MO-IX	R500C	ZD	0.18	1.05	0.049	19.58	30.99	445.3	4.47	1.63	-15.19		
MO-IX	R368B	CCD_I	0.03	0.88	0.064	21.78	29.53	384.6	1.87	1.33	-14.94		
MO-IX	R371A	Zn	0.17	0.68	0.054	0.23	0.28	117 775.0	7.01				
MO-IX	R373A	CCD_I	0.42	0.76	0.050	21.05	30.28	4 451.2	7.48				
MO-V	R358A	CCD_II	0.03	0.01	0.019	22.12	29.45	253.0	1.14	-0.61	-17.12		
MO-V	R359A	CCD_I	0.04	0.58	0.051	20.49	28.99	324.8	1.08	1.06	-13.17		
MO-V	R356B	CCD_I	0.05	1.63	0.079	21.69	30.44	102.5	1.15	1.17	-12.57		
MO-V	R360A	Zn	0.03	1.03	0.048	18.24	28.58	31 829.6	1.44	-0.58	-12.26		
MO-VII	R319A	CCD_II	0.03	0.06	0.020	18.79	36.01	13.9	1.32	0.32	-18.29		
MO-VII	R320A	CCD_I	0.02	0.44	0.039	21.78	30.02	7.3	0.87	1.12	-16.43		49.85
MO-VII	R319B	CCD_I	0.07	0.92	0.059	19.75	33.55	9.0	1.56	0.95	-15.12		
MO-VII	R325A	CCD_I	0.02	0.66	0.067	22.02	29.76	7.2	1.14	1.13	-13.69	0.708267	50.18
MO-VII	R334B	CCD_II	0.02	0.07	0.038	21.18	32.00	82.5	1.35	1.37	-18.57		
MO-VII	R345B	CCD_I	0.02	0.41	0.043	21.48	30.42	7.2	1.44	1.34	-15.11		50.19
MO-VII	R345A	CC_I	0.02	0.06	0.016	1.49	56.19	3.8	0.92	1.67	-13.99		
MO-VIII	R350B	WC	0.01	0.00	0.006	0.36	55.95	3.1	4.26	0.82	-17.09		
MO-VIII	R354A	CCD_I	0.03	0.60	0.060	22.24	30.94	5.0	1.29	1.04	-14.87		
MA-I	R411B	CCD_II	0.12	0.05	0.024	20.38	30.87	21.6	0.74	0.78	-18.76		
MA-I	R411A	CCD_II	0.02	0.01	0.027	21.17	30.05	6.2	0.77	0.08	-17.49		
MA-I	R394A	WC	0.03	0.01	0.008	0.32	56.57	7.4	1.85	1.22	-17.29		
MA-I	R398A	WC	0.01	0.01	0.008	0.30	55.77	11.6	1.65	1.00	-17.07		
MA-I	R398B	CCD_I	0.02	0.79	0.063	21.01	29.89	17.6	2.38	1.04	-14.53		50.19
MA-I	R393B	LS	0.17	0.19	0.015	3.52	50.94	46.5	4.73	1.75	-14.49		
MA-I	R411C	DEDOL	3.62	1.72	0.032	11.85	36.23	43.2	7.65	-2.64	-10.72		
MA-II	R413A	CCD_II	0.05	0.13	0.027	20.98	31.75	4.1	0.69	1.34	-18.99	0.708152	
MA-II	R416B	CCD_I	0.05	1.13	0.086	21.95	33.15	8.5	1.67	1.2	-14.57		
MA-II	R416A	CCD_I	0.03	0.84	0.066	21.50	30.38	5.2	0.86	1.21	-14.36		
MA-III	R383A	CCD_II	0.02	0.01	0.016	22.33	31.32	8.7	0.39	0.47	-18.09		
MA-III	R383B	CCD_I	0.35	0.58	0.019	19.61	33.19	59.3	5.58	0.43	-16.65		
MA-III	R382B	CCD_I	0.03	0.26	0.032	22.41	29.35	9.7	1.79	0.31	-16.13		51.59
MA-III	R382A	CCD_I	0.32	0.93	0.035	21.99	28.52	35.3	3.00	0.97	-16.12		50.48
MA-III	R378A	CCD_I	0.03	1.27	0.067	20.63	31.94	36.9	5.44	1.07	-14.44		

3 RESULTS

3.1 Field Observations

The Ranero and El-Moro/El-Mazo study areas are separated by the Karrantza valley *(Fig. 4)*. In both areas, dolomite bodies can easily be differentiated by their dark grey color as compared to off-white host limestone *(Fig. 5a)*. In the eastern sub-area (Ranero), different outcrops were studied namely a dolomite occurrence in the Pozalagua quarry, called "quarry" *(Fig. 5b)*, a 15-20 m thick dolomite body along the Ranero fault (sometimes also called Pozalagua fault) called "fault"

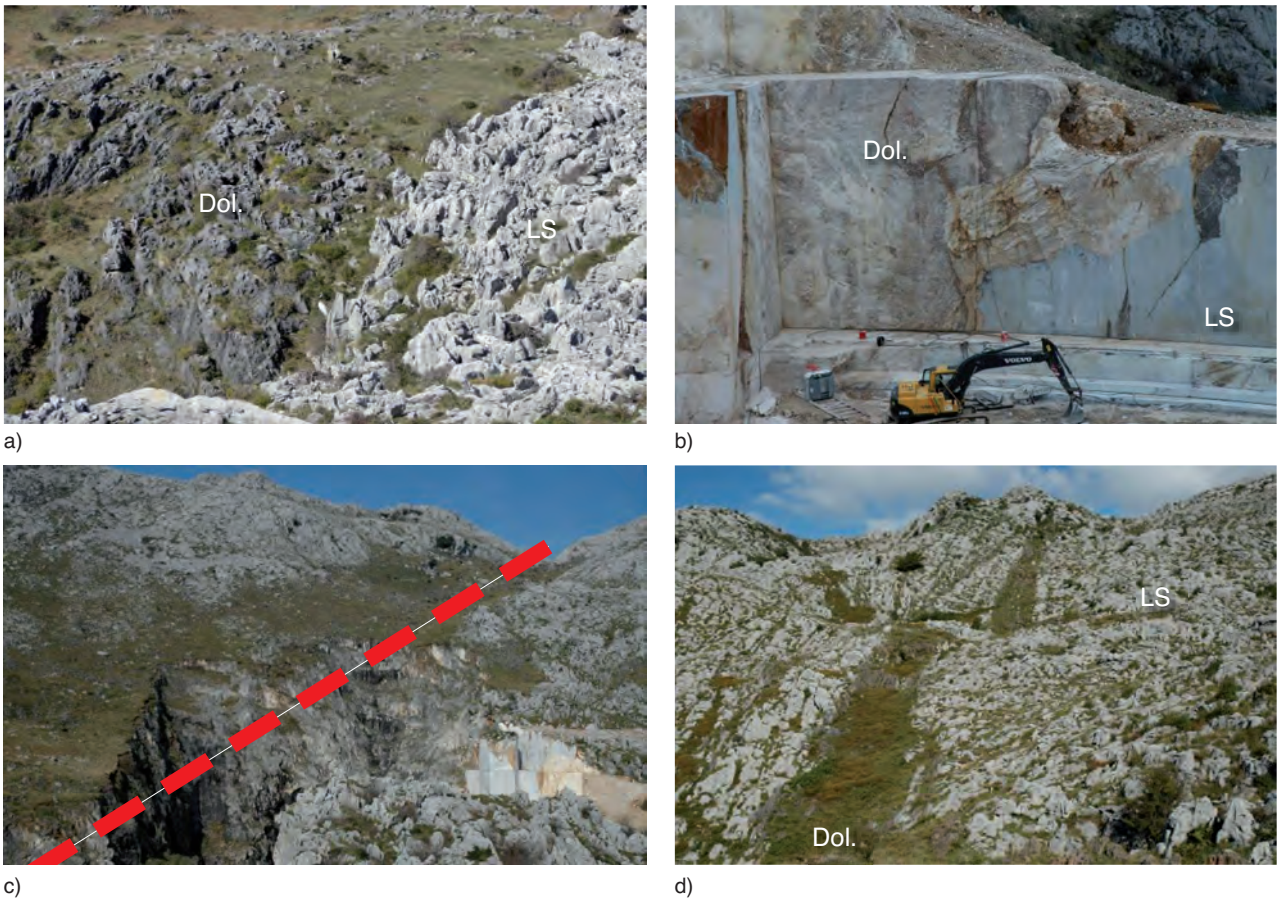

Figure 5

Dolomite bodies in the Ranero area. a) Color contrast between dolomite and limestone. b) Pozalagua quarry. c) General view of the Ranero dolomite body along the fault (dash line). d) Dolomite vein in the host limestone, west of Pozalagua quarry.

(Fig. 5c), inter-fingered dolomite body in the limestone called "front", a road side cataclastic limestone cemented by dolomite (called "breccia") and a >20 m thick vein dolomite called "vein" *(Fig. 5d)*. In the western sub-area (El-Moro), a 30 m thick dolomite body was studied at three different locations (MO-I to MO-III) to understand the vertical variations in the same dolomite body *(Fig. 6a)*, exposing fault-related features (striations) along with white colored calcite (MO-III section, *Fig. 6b*). The two next dolomite bodies (MO-IV and MO-V) occur in the central part of the El-Moro area, while a few others (MO-VII and MO-VIII) outcrop in the valley between El-Moro and El-Mazo areas *(Fig. 4, 6a)*. Dolomite bodies studied in the western extremity of the El-Moro area include MO-IX and MO-X *(Fig. 4, 6c)*. Mostly, these dolomite bodies are yellowish-brown to dark grey, crumbly weather colored and restricted to faults and fractures and exhibit more than 1 km linear extension. Besides, lateral distribution of these dolomite bodies are also evident (~500 m) in some localities of the study area.

Fault-related dolomite bodies are generally oriented N-S, NW-SE and NE-SW. They show variation in their textural distribution across the fault as dolomitisation can range from saddle dolomite in and around faults and fractures to pervasively dolomitised margins and considerably massive dolomitised bodies (Shah *et al.*, 2010). Dolomite veins also existed in the host limestone as their density decreases away from the main dolomite body. Besides various phases of dolomite, white to transparent calcite mostly occurs along the borders of the dolomite bodies in the study area.

Excellent dolomite exposures in the Pozalagua quarry site show different diagenetic phases (dark to light grey, brown to yellowish, pinkish and milky white to light pink) and hence may confirm the repetitive expulsion of dolomitising fluids along the Ranero fault (Swennen *et al.*, in press).

3.2 Diagenetic (Micro) Facies

The present study only focuses on dolomitisation events in the host limestone, since the early limestone diagenesis has

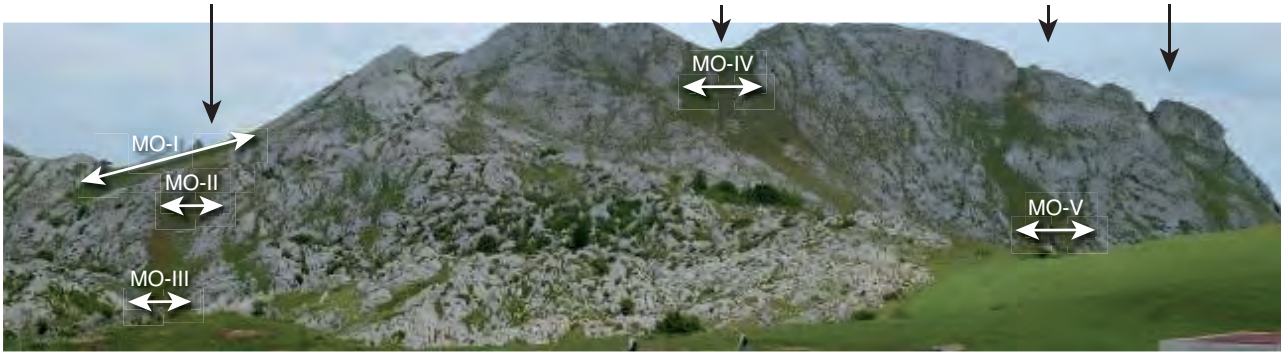

a)

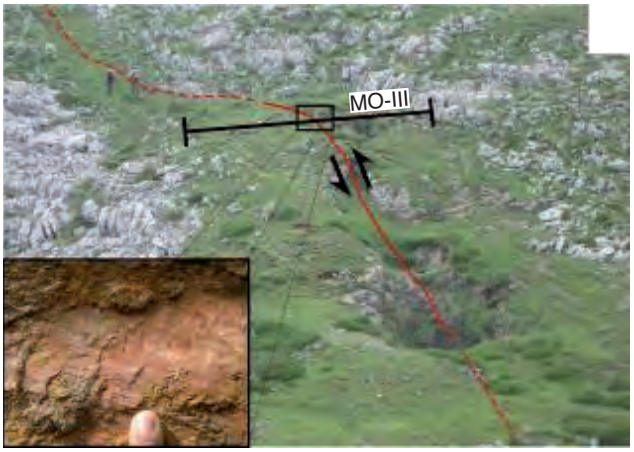

b)

c)

Figure 6

Dolomite bodies in the El-Moro area. a) Multiple dolomite corridors (black bold arrows) in the El-Moro area, where various sections were studied and sampled. b) Corridor along the fault in the El-Moro area with inset showing fault striations. c) Dolomite corridor in the eastern part of El-Mazo area.

been described in detail by Lopéz-Horgue *et al*. (2009 and 2010) and Rosales and Pérez-Garcia (2010). Various calcite and dolomite phases were distinguished on the basis of excellent exposures and petrographic studies. These include: cavity-filling calcite cement (CC-I and CC-II); medium to coarse crystalline dolomite (CCD-Ia and CCD-Ib); coarse crystalline saddle dolomite (CCD-II); White Calcite cement (WC) and Transparent Calcite (TC). Bed parallel and an oblique generation of stylolites were observed in host limestone. The oblique stylolite system was also seen in the calcite and dolomite phases. CC-II calcites record various episodes of fracture activation, while brecciation of late stage dolomite (CCD-II) is also reported before the emplacement of White Calcite cement (WC). Further brief description of each calcite and dolomite phase is given below.

3.2.1 Cavity-Filling Calcite Cements (CC-I and CC-II)

In the study area, cavity-filling, bladed calcite cement (CC-I) developed along the borders of the cavities of the host limestone and the crystals are oriented towards the centre of the cavity, while coarse crystalline calcite (CC-II) filled the remaining cavity except the central part, which may be filled by late stage dolomite and/or calcite *(Fig. 7a)*. Such calcite (CC-I and CC-II) filling is restricted to host limestone. Microscopic observations of the samples collected from the Pozalagua area show bladed and coarse crystalline early calcite cement (CC-I and CC-II), which occur in contact with host limestone *(Fig. 7b)*. The bladed calcite (CC-I), usually 300 μm to a few millimetre in diameter, possesses a dull red luminescence. The CC-I crystals are elongated and pointed towards the coarse crystalline, non-luminescent calcite (CC-II; *Fig. 7b*). In contrast to the Pozalagua area, the early cavity-filling calcite (CC-I and CC-II) has only been observed in a few locations of the El-Moro area (MO-I, III and VII). Oblique stylolites have been observed in the cavity-filling calcites (CC-I and CC-II), hence indicating their formation prior to regional burial according to the burial curve of Lopéz-Horgue *et al*. (2010).

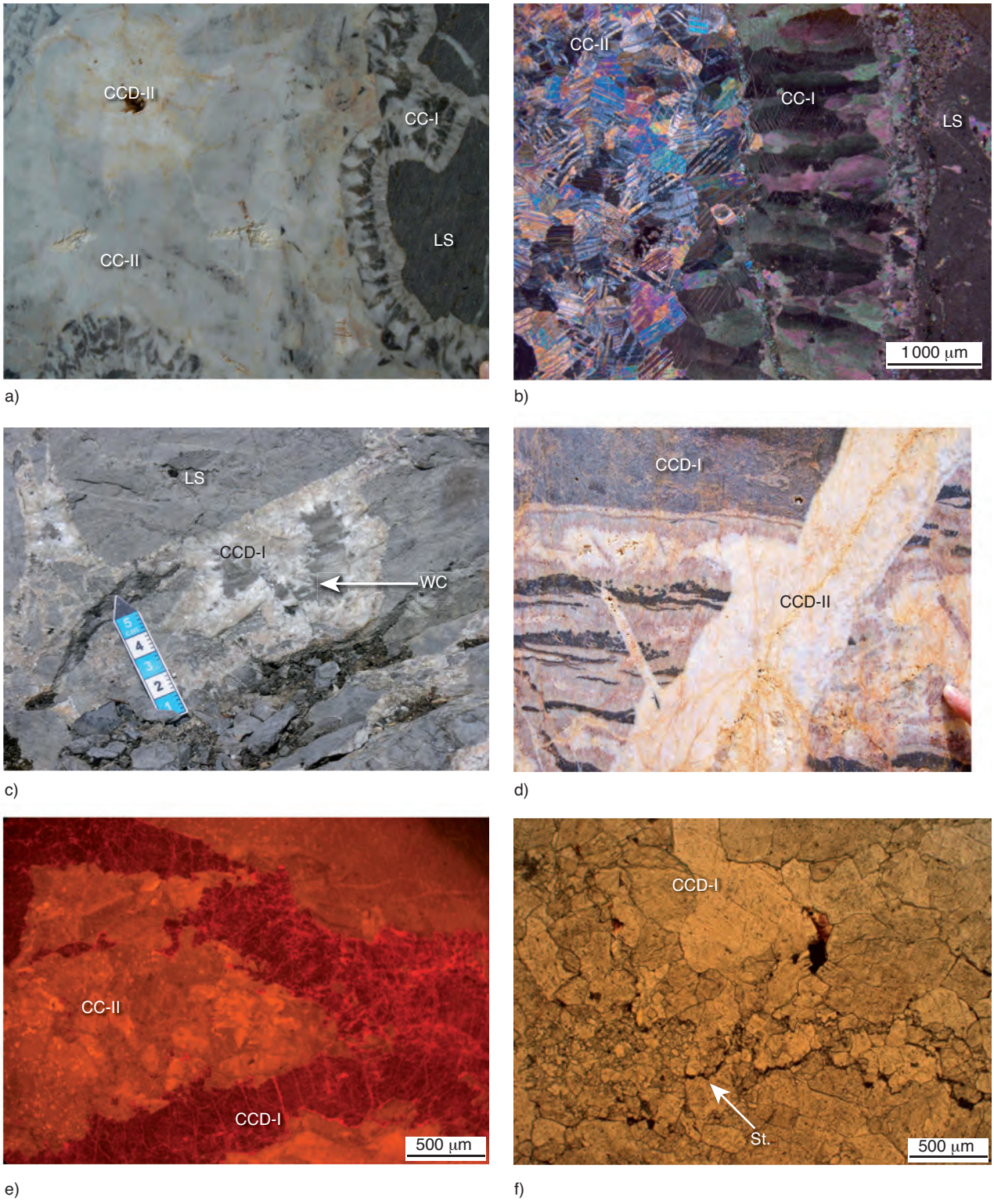

Figure 7

Cementation stages in the Ranero and El-Moro areas. a) Karst filling calcite (CC-I & CC-II) in the host limestone, note that open spaces are filled by CCD-II. b) Photomicrograph showing bladed, unidirectionally oriented CC-I in contact with randomly distributed CC-II and host limestone. c) In the Ranero breccia, calcite-filling (WC) after CCD-I. d) Late stage CCD-II cross-cutting and invading CCD-I in Ranero quarry. e) CL photomicrograph showing medium to coarse crystalline dolomite (CCD-I) cutting early, cavity-filling calcite (CC-II). f) Stylolite occurrence in dolomite (CCD-I).

3.2.2 Medium to Coarse Crystalline Dolomite (CCD-Ia and CCD-Ib)

In the breccia zone, fault reactivation resulted in brecciating the limestone into clasts, with medium to coarse crystalline dolomite (CCD-I) surrounded these clasts while open spaces are filled by White Calcite *(Fig. 7c)*. These medium to coarse crystalline dolomites (CCD-I) mostly consist of alternating bands of various colors (brown, grey and white) and Fe-rich layer bordering the walls of the vein and open cavities *(Fig. 7d)*. Microscopically, they appear as medium to coarse crystalline, nonplanar interlocking dolomite crystals. The CCD-I dolomites occur in almost all the studied sections and post-date cavity filling, coarse crystalline calcite (CC-I; *Fig. 7e*). They are further sub-divided into Fe-rich, dark colored, dark orange (in CL) rimmed saddle dolomite (CCD-Ia) and grey colored, dull luminescent saddle dolomite (CCD-Ib), which terminate in interstitial pores *(Fig. 8d, e)*. Selective dedolomitisation of the Fe-rich part of the coarse crystalline dolomite (CCD-Ia) is observed. These pore spaces are filled by very coarse to coarse crystalline, pore filling dolomite (CCD-II), which also replaces CCD-I, locally. Pyrite (now often oxidised) occur in the pores and along the fractures and in the stylolites present in CCD-I *(Fig. 7f)*.

3.2.3 Coarse Crystalline Saddle Dolomite (CCD-II)

Milky white to light pink colored coarse crystalline saddle dolomite (CCD-II), usually plugs the cavities in CC-II and cross-cut host limestone and CCD-I *(Fig. 7a, d)*, sometimes replacing CCD-I. On the basis of cross-cutting relationship, CCD-I pre-dates CCD-II, hence formed during a first dolomitisation stage *(Fig. 7d)*. It is also observed that CCD-II post-date all the dolomite phases in the quarry site *(Fig. 7d)*. The termination of dolomite event is marked by the deposition of pyrite along the borders of CCD-II *(Fig. 8a)*. Microscopic observation revealed that such late stage dolomitisation consist of coarse to very coarse crystalline nonplanar and dull luminescent saddle dolomite (CCD-II). Such dolomite mostly occurs as vein- and/or fracture filling and does not alter the host limestone, but can replace CCD-I dolomite *(Fig. 8b)*. Such dolomite phase was best exposed in the Pozalagua quarry site.

3.2.4 Coarse Crystalline, Pore-Filling White Calcite Cement (WC)

After the dolomitisation event, further cataclastic deformation (brecciation) resulted locally in the breakdown of dolomite into clasts, shortly after filling of open spaces by coarse crystalline, pore and vein-filling White Calcite (WC; *Fig. 8a*). Petrographic studies show distinct crystal twinning behavior of these coarse crystalline calcite, indicating exposure to tectonic stresses (Swennen *et al*., in press). CL studies of these pore-filling, White Calcite (WC) revealed dull-luminescence and formed after the dolomitisation stage (usually surrounds broken dolomite fragments). White Calcite (WC) is widespread in all the studied sites *(Fig. 8c)*.

3.2.5 Medium to Coarse Crystalline, Transparent Calcite (TC)

Transparent to dirty white calcite (TC) usually occur as latest pore- and vein-filling phase. Microscopically, medium to coarse crystalline, pore-filling Transparent Calcite (TC) exhibits non-luminescence. Such calcite is quite common and mostly responsible for reduction/destruction in porosity as it occludes open spaces in dolomite *(Fig. 8d)*. Besides this, dedolomitisation of coarse crystalline dolomite (CCD-I) is mostly associated with this calcite.

3.2.6 Replacive Dolomites (ZD and DS)

Beside the above stated dolomite cements, dolomite also occurred as a replacement product of the host limestone in zebra and in pockets of layered, pink sucrosic rocks interpreted as dolomitised internal sediments (DS) of a cave system *(Fig. 9a, c)*. Zebra Dolomites (ZD) mostly consist of inter-layered planar to nonplanar, fine to medium- crystalline dolomite matrix and nonplanar, coarse crystalline dolomite cement phases, giving zebra-like texture *(Fig. 9b)*. Zebra Dolomites mostly occur next to faults and fractures adjacent to the fault, quarry, breccia and vein sections but they were not observed in the front section in the Ranero area. In the El-Moro area, Zebra Dolomite is not as common as observed in the Ranero area and was only identified in MO-I and MO-II sections. Dolomite Sand (DS) consists of medium to coarse crystalline, nonplanar dolomite, clays and pyrite *(Fig. 6f)*. These rocks display a laminated texture at the hand specimen scale and invariably contain much more silicate impurities that the other dolomites (up to 2% Al_2O_3; *Tab. 1* and Nader *et al*., in press). Silicates (illite, chlorites) are grouped with pyrite in the residual space between dolomite crystals. This lithotype is best exposed in the quarry site as paleo-cavity filling dolomites and more difficult to identify in the other places.

3.2.7 MVT-Type Mineralisation

MVT-type mineralisation (Galena-Barite and Sphalerite-Galena) was also observed near the studied sites. Galena-Barite mineralisation is observed in one single vein from the Ranero area, within a marly carbonate host (slope facies). Sphalerite-Galena mineralisation is absent in the Ranero area, but present by places in El Moro area; it is always hosted in CCD-I dolomite bodies. Primary sphalerite-galena mineralisation is rarely preserved, but it seems to predate or to be coeval with CCD-I dolomite; secondary mineralisation including smithsonite (bright blue colored in CL; *Fig. 9d*) and Pb-rich calcites is more frequently observed in El Moro area, but it clearly postdates dolomite.

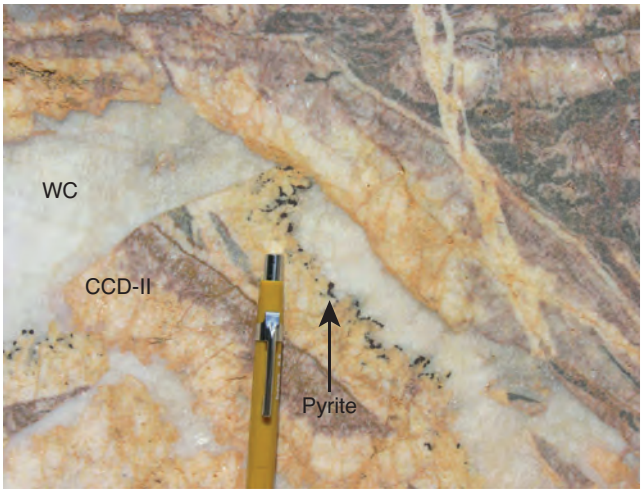

a)

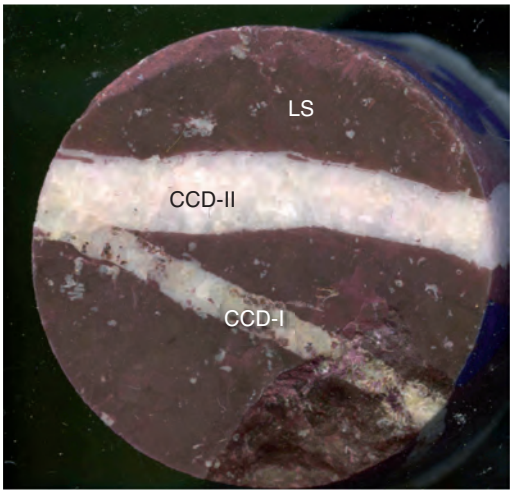

b)

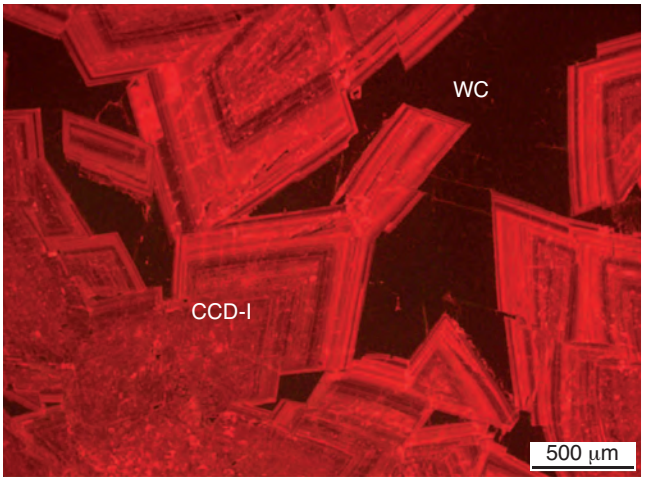

c)

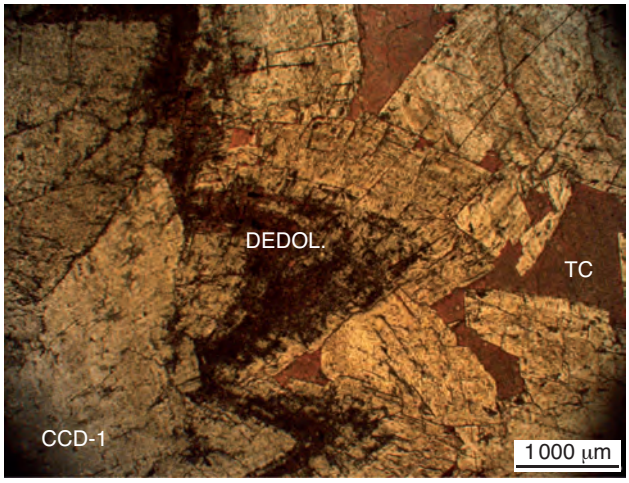

d)

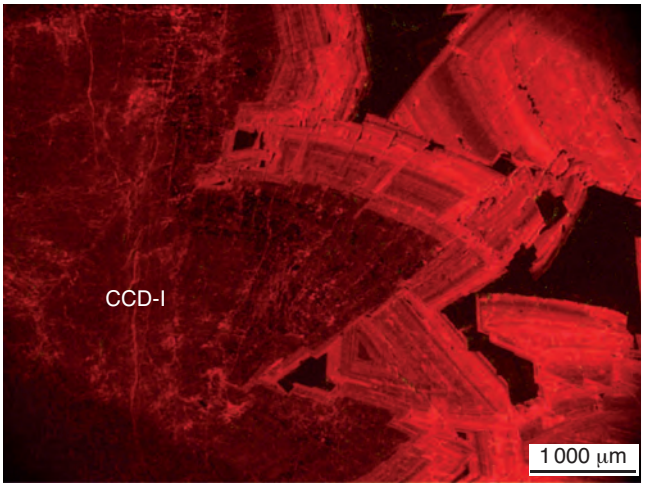

e)

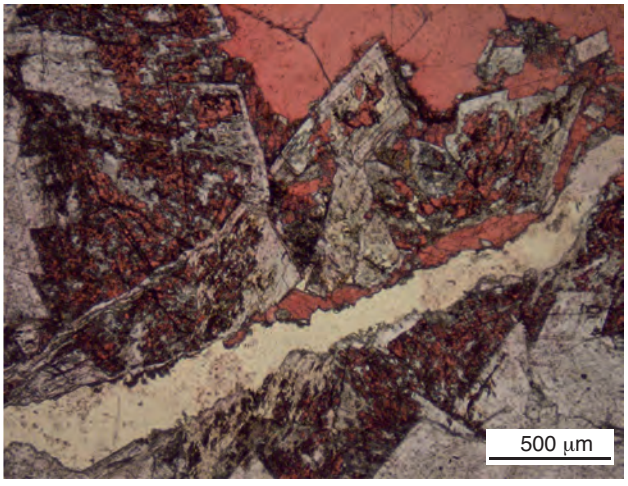

f)

Figure 8

Petrographic properties relative to age relationships. a) White calcite vein containing dolomite breccia (CCD-II). b) Sampled plug showing cross-cutting relationship of CCD-I and CCD-II in host limestone. Vertical bar = 1.5 cm. c) CL photomicrograph showing late stage, zoned dolomite (CCD-II), while late stage White Calcite (WC) filling the intercrystalline pore spaces. d) & e) PPL and CL photomicrographs of early, dolomite (CCD-I), showing a selectively dedolomitised zone and pore-filling late calcite (TC). f) Late stage dedolomitisation related to red-stained calcite (TC).

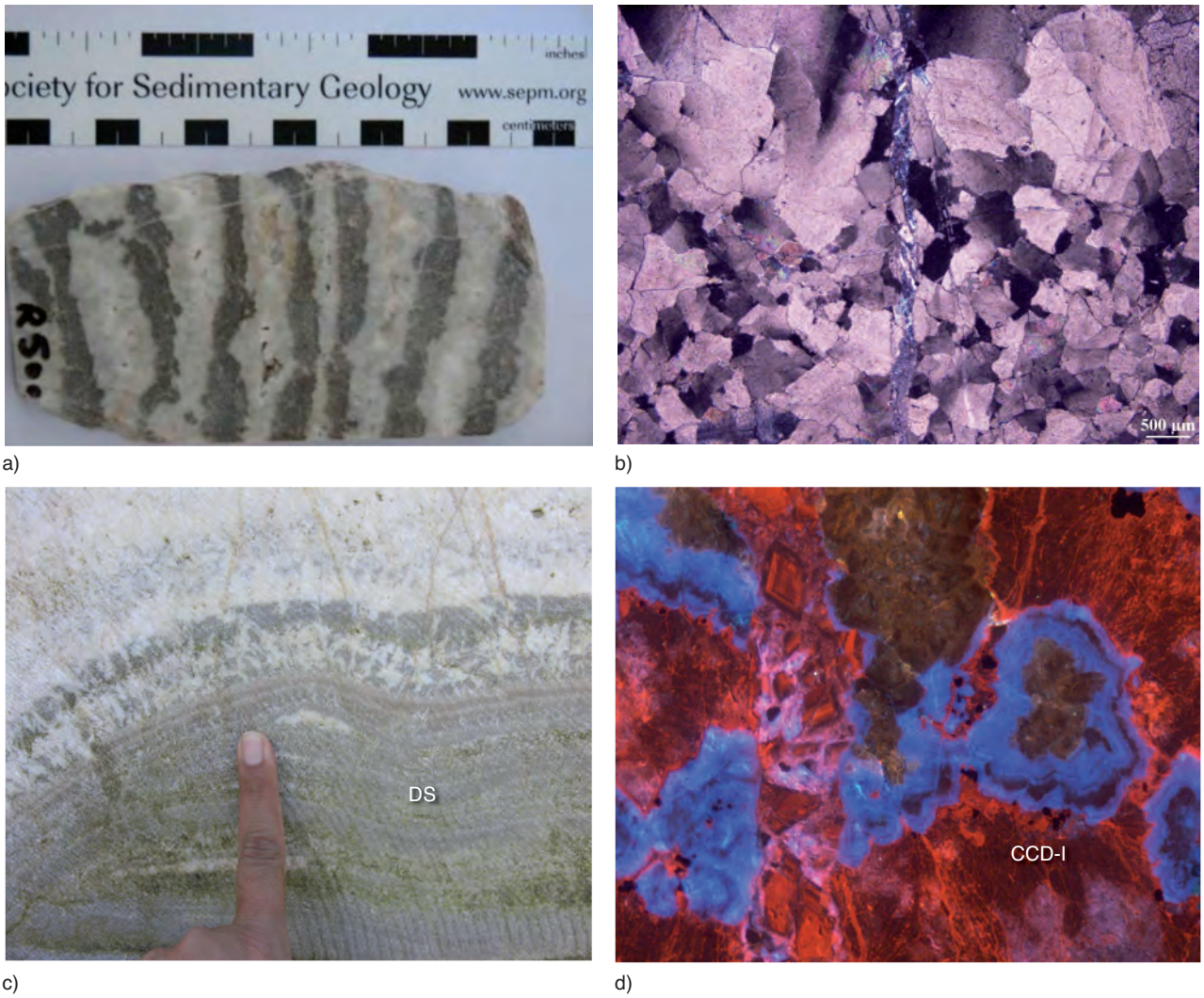

Figure 9

Field and petrographic observations showing replacive dolomites. a) & b) Hand specimen showing interlayered dark grey and dirty white dolomite, while photomicrograph showing coarse and medium to fine crystalline dolomite exhibiting zebra texture. c) Laminated dolomitised internal sediments (DS). d) Sphalerite mineralisation observed in the ferroan dolomite (CCD-I).

3.3 Stoichiometry and Geochemical Attributes

In order to know the mineralogical and chemical characteristics of the identified dolomite and calcite phases, X-ray diffraction studies as well as geochemistry of major and trace elements were carried out. Dedolomitisation, as an example of diagenetic processes, is also favored by nonstoichiometric dolomites (Dorobek *et al*., 1993; Nader *et al*., 2008). For this purpose, initially X-ray diffractometry was used to determine the stoichiometry of the selected dolomite phases. All the dolomite samples analysed exhibit sharp diffraction peaks. The d104 spacing is quite constant and ranges between 2.8863 and 2.8912 Å. These d104 spacing values correspond to a Ca content between 50.1 and 51.7 mol%, hence exhibited stoichiometric behaviour (Lumsden, 1979).

3.3.1 Major and Trace Elements

Various dolomite facies are grouped on the basis of their major and trace element contents. FeO contents in various dolomite phases helped in categorising them into ferroan (> 0.2%) and non-ferroan (< 0.2%; *Fig. 10a, b*). Fe-rich dolomite mostly coincide with the initial phase of pervasive, medium to coarse crystalline saddle dolomite (CCD-I), which is further sub-divided into CCD-Ia (Fe- rimmed; ~ 1% Fe) and CCD-Ib (band-filling; ~ 0.5% Fe). The FeO-contents in coarse crystalline, vein- and fracture- filled, non-ferroan dolomite (CCD-II) ranges from 0.2% to 0 *(Fig. 10a, b)*. The

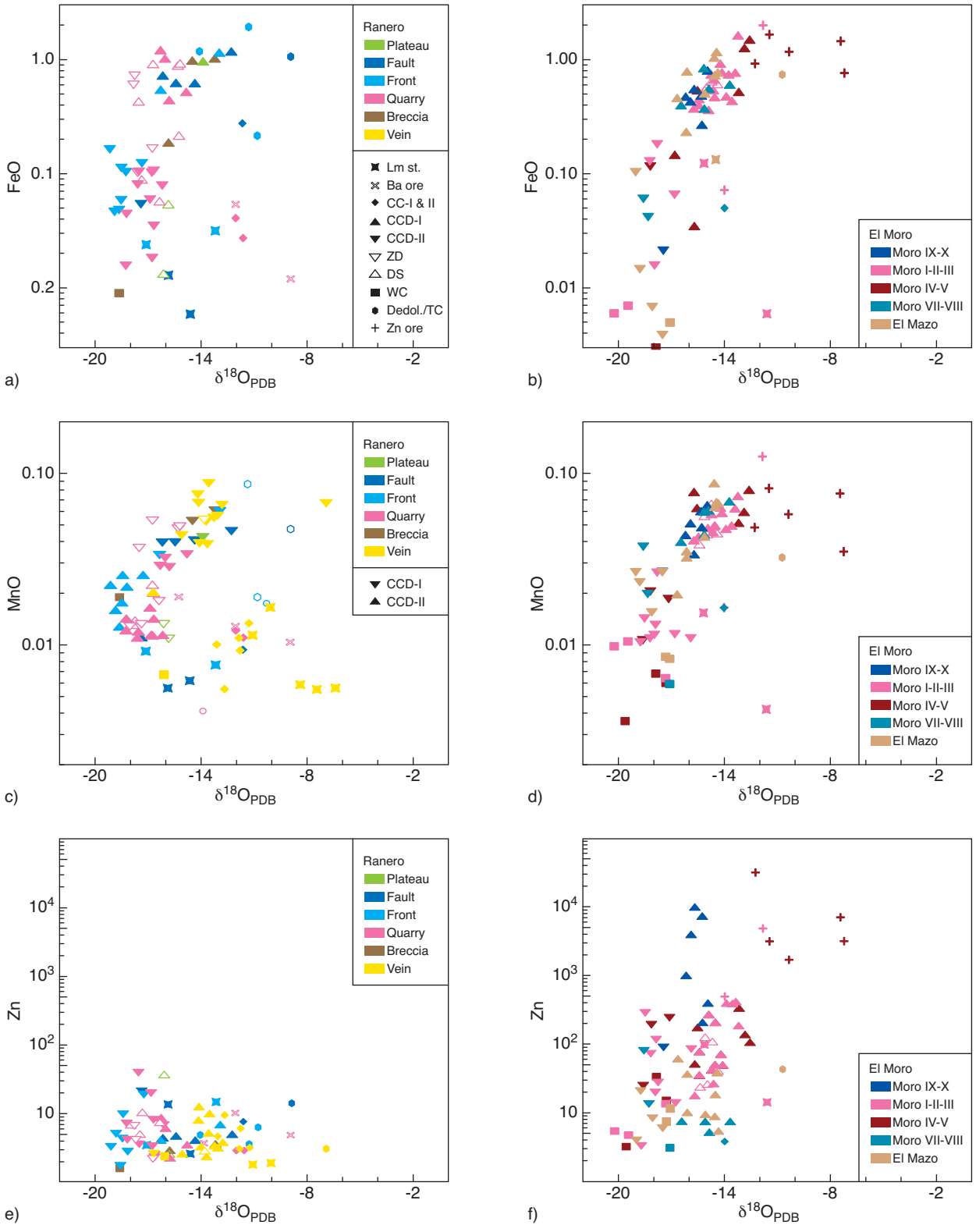

Figure 10

Geochemistry of hydrothermal minerals, limestones and replaced rocks in the Ranero (left side) and El-Moro (right side) areas.
a) & b) FeO- *vs* $\delta^{18}O$ crossplot showing the compositional shift of successive dolomite stages. c) & d) Mn- contents. e) & f) Zn- enrichment in parts of the El-Moro area contrasts with the barren Ranero dolomites. Note that all the Zn-rich samples have a high FeO content suggesting a link with CDD-I. Legend in a) serve as well for Figure 11.

crossplot $\delta^{18}O$ *vs* FeO shows contrast between Fe-rich dolomite (CCD-Ia and CCD-Ib) and non-ferroan dolomite (CCD-II). In the Ranero vein section, Fe-rich dolomite (CCD-Ia and CCD-Ib) is abundant, while non-ferroan dolomite is rare. On the other hand, both the Fe-rich and non-ferroan dolomites are reported in all the other studied sites (plateau, fault, front, quarry and breccia; *Fig. 10a*). Dedolomitisation almost selectively affects the ferroan rich dolomite in the Ranero front section. Galena-Barite vein is associated with the non-dolomitised limestone near the Pozalagua quarry.

In the El-Moro area, pervasive, ferroan dolomite and vein-filling, non-ferroan dolomite occur in all the studied sections *(Fig. 10b)*. However Fe-rich, medium to coarse crystalline dolomite (CCD-I) largely dominates in the western part (Moro I to III and Moro IX-X sections). In the central and eastern part (Moro IV-V, Moro VII-VIII and El-Mazo), both the ferroan and non-ferroan dolomite phases are present. Galena-Sphalerite and the secondary Zn-Pb mineralisation are mostly observed in the central part of the El-Moro area within ferroan dolomite bodies.

The Fe- and Mn-contents are proportional to each other in the studied dolomites (Ranero and El-Moro areas), hence Fe-rich dolomite (CCD-I) shows high Mn-contents as compared to non ferroan dolomite (CCD-II; *Fig. 10c, d*). Besides, dolomites containing substantial amounts of Zn shows high Mn- contents and is ferroan *(Fig. 10f)*. In the Ranero area, ferroan dolomite exhibited negligible Zn mineralisation, while in the El-Moro area show high Zn-contents are reported from the western (MO I-II-III and MO IX-X) and central parts (MO IV-V), while the eastern part (MO VII-VIII and El Mazo) appears to be less affected by Zn mineralisation *(Fig. 10e, f)*. Zn-rich dolomite samples are also Fe-rich and are particularly prone to dedolomitisation.

3.3.2 Stable Isotopes

In the studied sites, various dolomite facies show broad range of depleted $\delta^{18}O$ values (–18.0 to –10.0‰ V-PDB), while their $\delta^{13}C$ values (0.0 to + 2.0‰ V-PDB) are close to the range of reported carbonates precipitating from early Albian seawater *i.e.*, 0.0 to + 4.0‰ V-PDB (Veizer *et al.*, 1999). However compared with the analysed limestones from our study area, which exhibit values of + 3.0 ± 1.0‰ $\delta^{13}C$, the dolomites show relatively depleted $\delta^{13}C$ values, which may indicate a possible external source of carbon during dolomite precipitation *(Fig. 11a, b)* or a temperature dependent fractionation effect. In order to explain depleted $\delta^{18}O$ values, it has been well documented that precipitation of dolomites from hot fluids leads to relatively depleted $\delta^{18}O$ compositions (Land, 1983). The analysed host limestone also shows considerable depletion in their $\delta^{18}O$ values (–17.10 to –4.5‰ V-PDB), which may be due to recrystallisation by hot fluids. Cavity-filling calcite cements (CC-I and CC-II) show almost the same distribution of depleted $\delta^{18}O$ (–14.02 to –10.06‰ V-PDB) and $\delta^{13}C$ (+ 0.53 to + 1.99‰ V-PDB) values in Ranero and El-Moro *(Fig. 11a, b)*. The Fe-rich coarse crystalline dolomite (CCD-I) show less depleted $\delta^{18}O$ values (–16.35 to –12.05‰ V-PDB) as compared to non-ferroan dolomite (–19.25 to –16.60‰ V-PDB), indicating different temperature of dolomitising fluids or/and involvement of a different fluid *(Fig. 11a, b)*. Vein- and pore-filling calcite (WC) shows highly depleted $\delta^{18}O$ values (–20.10 to –16.05‰ V-PDB; *Fig. 11a, b*). In the Ranero area, carbonates associated with Galena-Barite mineralisation show similar

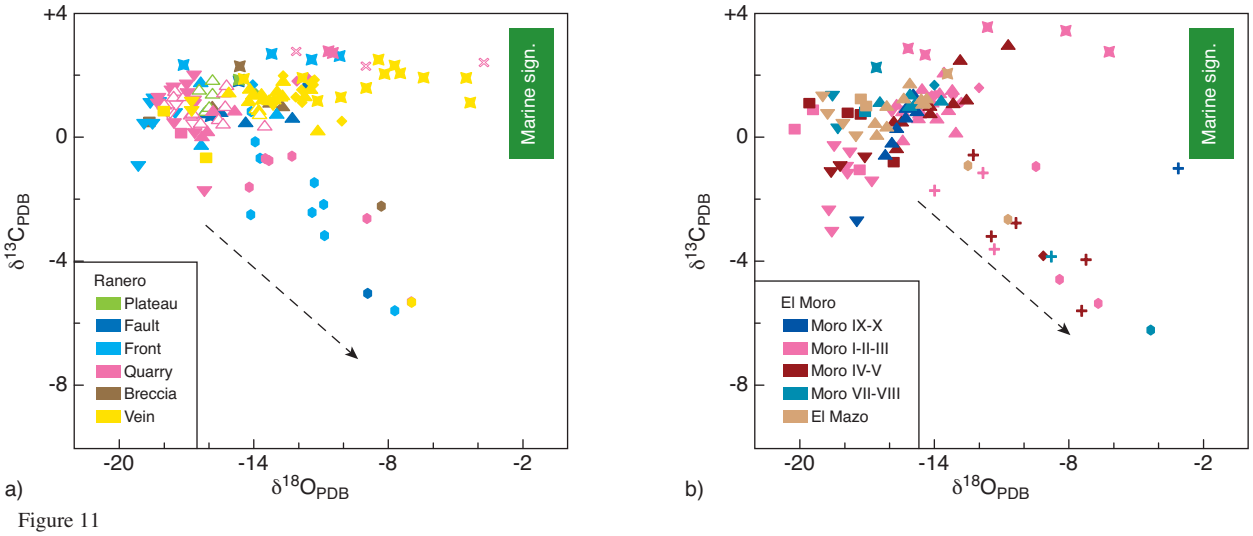

Figure 11

Stable isotope geochemistry. $\delta^{18}O$ *vs* $\delta^{13}C$ crossplot showing depletion in $\delta^{18}O$ and $\delta^{13}C$ values in both the studied sites and a slightly more depleted $\delta^{13}C$ in CCD-II from the El-Moro area.

$\delta^{13}C$ values as host limestone, indicating a buffered system, but the depleted $\delta^{18}O$ values indicate involvement of hot or depleted dolomitising fluids *(Fig. 11a)*.

It is noteworthy that dedolomitised facies show less depleted $\delta^{18}O$ values and highly depleted $\delta^{13}C$ values. Dedolomitised samples represent intimate mixtures between dolomite and calcite. In these samples, $\delta^{13}C$ depletion increases with calcite abundance, generating a mixing line whose depleted end-member is isotopically similar to Transparent Calcite (TC, *Fig. 11a*). This strongly suggests that the dedolomitisation process is coeval with Transparent Calcite deposition and involves surface-derived fluids contaminated by soil-CO_2. In the El-Moro area, Sphalerite-Galena associated dolomites show less depleted $\delta^{18}O$ (–13.99 to –3.11‰ V-PDB) and $\delta^{13}C$ values (–5.58 to –0.58‰ V-PDB), which corresponds to its association with dedolomitised rim in the Fe- rich dolomite as stated in the previous section *(Fig. 11b)*.

3.3.3 Strontium Isotopes

The $^{87}Sr/^{86}Sr$ *versus* $\delta^{18}O$ cross plot *(Fig. 12a)* shows that $^{87}Sr/^{86}Sr$ ratio and $\delta^{18}O$ values of the host limestone corresponds to 0.70741 and –4.45‰ V-PDB respectively, which lies within range of the $^{87}Sr/^{86}Sr$ signatures (ca. 0.70731 to 0.70745) of the original marine early to late Albian carbonates (McArthur *et al.*, 2001). The $^{87}Sr/^{86}Sr$ values of pore-filling early calcite (CC-I and CC-II) ranges from 0.70844 to 0.70852, while early stage, Fe-rich dolomite (CCD-I) exhibits $^{87}Sr/^{86}Sr$ values from 0.70827 to 0.70847. In contrast, the $^{87}Sr/^{86}Sr$ values of late stage non-ferroan dolomite (CCD-II) ranges from 0.70813 to 0.70826, while late stage White Calcite (WC) shows $^{87}Sr/^{86}Sr$ values in the range of 0.70877 and 0.70881. The above stated data indicate that most of the various dolomite and calcite phases are clustered and exhibits higher $^{87}Sr/^{86}Sr$ ratios compared to the original Sr-isotope marine signature. In addition, the presence of oblique stylolites in these dolomite phases invoke their formation prior to latest deformation during burial. Thus the relatively high $^{87}Sr/^{86}Sr$ ratios of the various investigated dolomites may indicate interaction of the dolomitising fluids with the radiogenic lithologies *(Fig. 12b)* during burial conditions prior to the formation of tectonic stylolites.

4 DISCUSSIONS

The NW-SE trending Pozalagua fault and other fractures, related to early Cretaceous (early Albian) rifting, appear to have been activated through sinistral strike-slip motion, followed by hydrothermal activity during late Albian to Turonian times (Thiébaut *et al.*, 1988; Aranburu *et al.*, 1994; Schärer *et al.*, 1999; Lopéz-Horgue *et al.*, 2010; Swennen *et al.*, in press). The elevated homogenisation temperatures of various dolomite phases (*i.e.*, 170 to 200°C) and burial history of the study area supported their hydrothermal origin

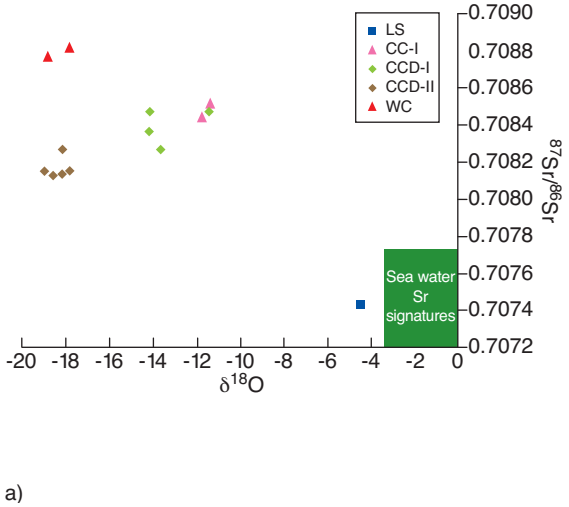

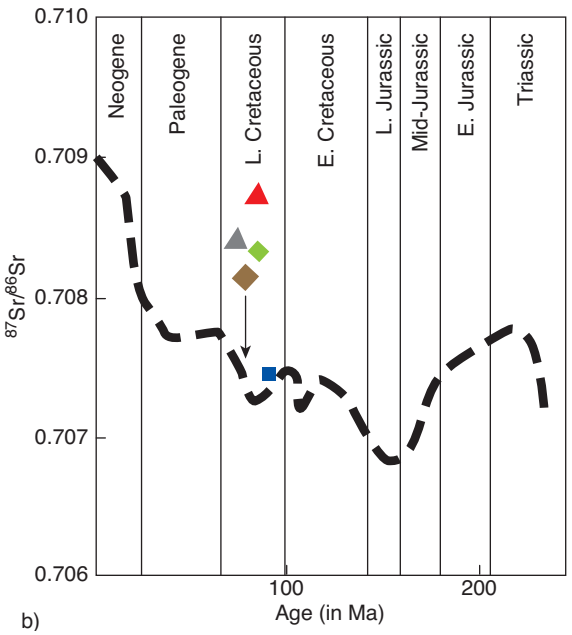

Figure 12

Sr isotope analyses. a) The $^{87}Sr/^{86}Sr$ *vs* $\delta^{18}O$ crossplot showing clear shift from the original marine signatures and indicate that dolomitising fluid interacted with radiogenic lithologies. b) Sr- curve indicating the position of various dolomite and calcite facies with respect to their ages.

(Lopéz-Horgue *et al*., 2010; Shah, 2011). The fact that the dolomite bodies are associated to faults indicates a tectonic control on the dolomite distribution (*Fig. 5, 6*; Garcia-Mondéjar, 1996; Lopéz-Horgue *et al*., 2005, 2010; Gasparrini *et al*., 2006; Shah *et al*., 2010; Swennen *et al*., in press). Various dolomite phases are believed to have formed due to the circulation of Mg-rich dolomitising fluids along faults/fractures, hence invoking multiple pulses of these fluids (Swennen *et al*., in press).

4.1 Chemistry of Dolomitising Fluids

Dolomite and calcite phases in the Ranero area show a broad range of depleted $\delta^{18}O$ values, while $\delta^{13}C$ values indicate slight shift from those of the analysed nearby host limestone. In the El-Moro area, relatively less dispersion in terms of $\delta^{18}O$ values and similarly depleted $\delta^{13}C$ values are observed *(Fig. 11a, b)*. The highly depleted $\delta^{18}O$ values may either be due to increase in temperature or/and ^{18}O-depleted fluids. The slight shift in $\delta^{13}C$ of dolomites with respect to the host limestone can be explained by the slight temperature fractionation of 0.03‰ per degree Celsius (Emrich *et al*., 1970). The estimated salinity of the primary inclusions of these dolomite facies are three to four time greater than seawater (12-21 eq. wt% NaCl; Shah *et al*., 2010). This piece of information together with the observed presence of sulphate phases (Bustillo *et al*., 1992) eliminates meteoric water as possible explanation for depleted $\delta^{18}O$ values. Other depleted fluids cannot be excluded but temperature increase is the likely cause for the depleted $\delta^{18}O$ values as argumented by the high T_h values. Broad range of these salinity values may indicate the presence and variable mixing of multiple dolomitising fluids as observed in MVT-type mineralisation (Leach *et al*., 2005). However some depleted values can also be possibly explained by contamination with calcite (TC) in the analysed samples (*Fig. 11a, b*; Emrich *et al*., 1970); this latter cement (*i.e*. TC) having a relatively depleted $\delta^{18}O$ signature.

Two episodes of dolomitisation resulted in ferroan dolomite (CCD-I) and non-ferroan dolomite (CCD-II). The origin of the hypogene karstification before Fe-rich dolomitisation is unknown, but one possibility could be "cooling of formation waters" (Giles and de Boer, 1989). Two possible sources of dolomitising fluids may be proposed, which include:

- permo-triassic siliciclastics, and
- deep basinal deposits.

Although permo-triassic siliciclastics acted as good aquifer for the fluid migration in other parts of the world, but the burial history shows much lesser ambient temperature (López-Horgue *et al*., 2010) as observed in the fluid inclusion studies (Shah *et al*., 2010). This eliminates siliciclastics of the permo-triassic age as possible source, hence dolomitising fluids originated from deep basinal deposits. So, Initial episode of Fe-rich dolomitising fluids may have liberated from the adjacent basinal deposits and resulted in precipitation of CCD-I. For the second episode of dolomitisation, the circulating fluids exhibited very high temperature as evidenced by the T_h values of the fluid inclusions (explaining also the highly depleted $\delta^{18}O$). In the Pozalagua quarry, the circulation of such high temperature fluids along faults/fractures which could be associated with flexuring in the Aptian-Albian limestone due to the presence of diapiric structures in the area (López-Horgue *et al*., 2010), succeeded in the formation of CCD-II. It can be speculated that such dolomitising fluids may be related to different sources, such as igneous activity and convective flow induced by the high temperature magmatic activity (Shah *et al*., 2010; Swennen *et al*., in press).

Sr isotope analyses indicate that the calcite and dolomite phases contain radiogenic signatures, which is evident by the clear shift from the marine early Cretaceous signatures *(Fig. 12a)*. Most of the dolomite phases possess a signature that varies from 0.70820-0.70850, which conclude that dolomitising fluids may have interacted with radiogenic lithologies (sandstones and shales) during late Albian intense tectonic activity, confirming the results of Bustillo *et al*. (1992) *(Fig. 12b)*.

4.2 Dolomite Distribution and Variations

Dolomite bodies are widely observed in the Ranero area, where pervasive dolomitisation extended more than 1 km along the Pozalagua fault and as much as 500 m wide in the north-western part of Ramales platform. Such extensive distribution of dolomite bodies in the Ramales area is believed to be due to the prior development of paleo-karsts as observed in the Pozalagua quarry. In contrast to this, dolomite bodies in El-Moro area are strictly confined to faults and fractures that developed at the platform edge to basin transition, and exhibits little vertical and lateral extension. Besides the variation in size of dolomite bodies in the Ranero and El-Moro, other remarkable contrasting features are:

- relatively broad range of $\delta^{18}O$ values in the Ranero area as compared to El-Moro area;
- Galena-Barite mineralisation observed in the Ranero area, while Sphalerite-Galena mineralisation is restricted to some parts of the El-Moro areas;
- in the El-Moro area, host limestone shows higher $\delta^{13}C$ values as compared to Ranero area;
- dedolomitisation is frequently found in both the studied sites, hence telogenetic processes can possibly can explain their formation.

Finally, it is worth stressing again that Ranero area exhibits a larger volume of dolomites, mainly associated to

the Pozalagua fault. While an earlier phase of dolomitisation (Fe-rich, originated due to compactional fluid flow) has been documented in this paper and interpreted as pervasively affecting the Ramales Platform, the later phase of dolomitisation (Fe-poor, associated to a thermal anomaly) appears to mainly affect the Ranero fault area.

4.3 Mechanisms of Dolomitisation

The Basque trough is an irregular graben-like feature developed adjacent to the Ramales platform (study area), where more than 8 500 m thick shales, sandstones and marls accumulated during upper Valanginian-late Cenomanian (Gibbons and Moreno, 2002). During burial, compactional dewatering may have resulted in hydrodynamic fluid flow along the NW-SE and NE-SW trending faults existing adjacent to the basin-platform margins (Vicente-Bravo and Robles, 1995). According to Bustillo *et al*. (1992), the dolomitising fluids originated in the NE of the basin from the mudrocks situated in the deeper part of the basin, where trapped sea water may have provided the Mg-rich fluids for dolomitisation. These hot, compactional fluids (120-200°C; according to Shah, 2008 and Lopez-Horgue *et al*., 2010) pervasively dolomitised the host limestone. During the burial of sedimentary basin and later hydrodynamic fluid flow, permeable carbonate platform limestones and faults/fractures control the extent of dolomitisation (Qing and Mountjoy, 1989). Such pre-requisites as permeable carbonate platform limestones, faults/fractures and paleo-karsts are present in the study area. The presence of linear (fracture-controlled) dolomite bodies supports the idea that the dolomitising fluids migrated and spread through the sedimentary pile along such discontinuities (Shah *et al*., 2010).

4.4 Hydrothermal Diagenesis and Dolomite Formation

Although a generalised paragenetic sequence was established in part of the study area on the basis of field observations, petrographic studies and stable isotope analyses (Shah *et al*., 2010), the present study involved a larger set of data including geochemical analyses allowing the elaboration of a detailed paragenetic sequence of the various dolomite and calcite phases and some more information about their spatial distribution *(Fig. 13)*. Non-ferroan dolomite were formed at relatively high temperature as indicated from fluid inclusion studies (Shah, 2008; Lopéz-Horgue *et al*., 2010). Fault reactivation resulted in brecciation of non-ferroan dolomite, creating voids that were later on filled by White Calcite

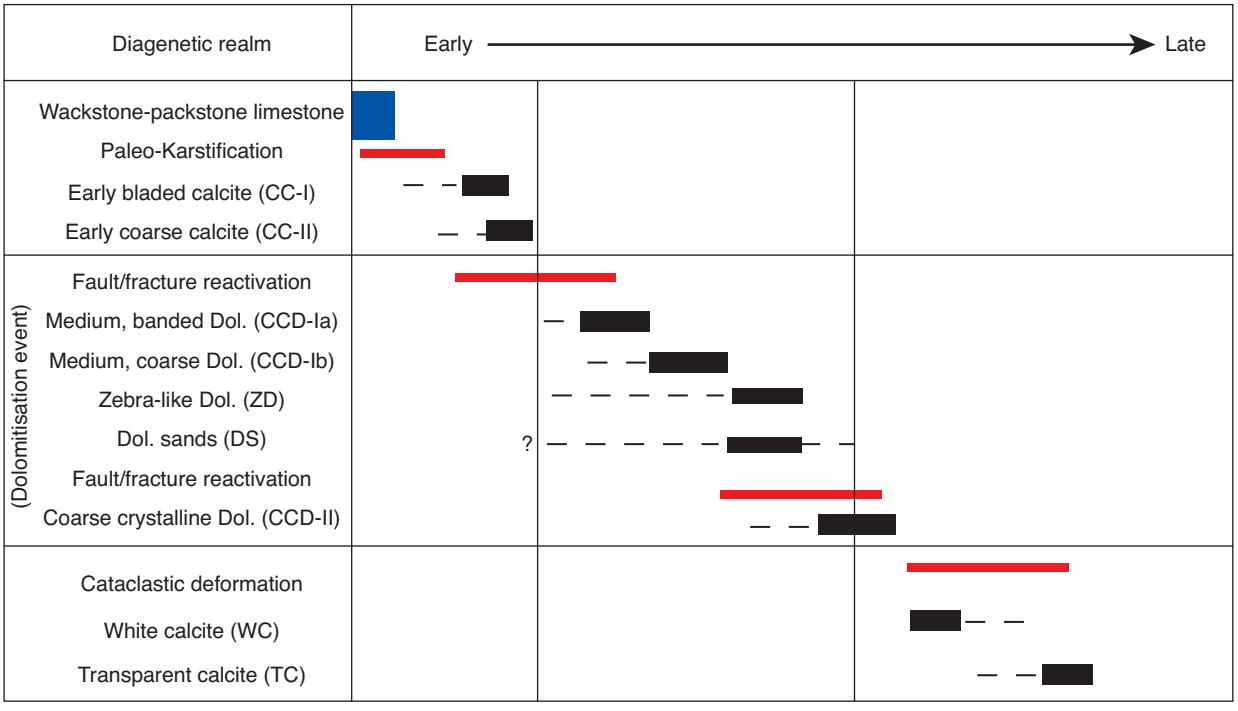

Figure 13

Proposed paragenetic sequence observed in the two studied sites (Ranero and El-Moro). Note that the red lines indicate events occurred during late diagenesis in the Albian carbonates.

(WC). Calcitised, non-luminescent part of CCD-I represent less depleted $\delta^{18}O$ and depleted $\delta^{13}C$ values *(Fig. 11a, b)*, likely formed near meteoric recharge (Choquette and James, 1988; Niemann and Read, 1988; Meyers, 1991; Reeder, 1991).

Cavity-filling calcite (CC-I and CC-II) represented an initial stage of hydrothermal activity prior to dolomitisation and showed less depleted $\delta^{18}O$ values compared to original marine signatures of Albian limestones *(Fig. 11)*. The first episode of dolomitisation (CCD-I) resulted from the influx of Fe- rich dolomitising fluids along reactivated faults/fractures, which regionally replaced the host limestone and calcite (CC-II) in particular, as was observed in the vein section. The process of replacement is evidenced by irregular (interfingur-ing) contacts between host limestone and dolomite. Fe-rich dolomite (CCD-I) seems to contain Sphalerite-Galena miner-alisation. Similar observations have been reported from the Réocin Zn-Pb deposits, situated NW of the study area (Symons *et al*., 2009; Velasco *et al*., 2003). Sphalerite-Galena associated dolomite phases in the Réocin area resulted in precipitation of Fe-rich dolomite in internal sedi-ments and in open spaces (sulphide deposition). This resem-bles with the Dolomite Sands (DS) in the study area. Zebra Dolomite (ZD) resulted from the replacement of host lime-stone. The second episode of dolomitisation (CCD-II) exhibits local scale vein-filling dolomites, which showed replacement of pre-existing dolomite (CCD-I). In contrary to CCD-I, non-ferroan dolomite (CCD-II) does not alter the host limestone substantially.

CONCLUSIONS

Field observations of the hydrothermal dolomites in the early Cretaceous basin-to-platform carbonates (Karrantza valley, NW Spain) including the development of a paragenetic sequence based on cross-cutting relationships, petrography, geochemical studies and isotope analyses resulted in the following conclusions:

– hydrothermal processes include (in paragenetic order) calcite precipitation (CC-I and CC-II), followed by two distinct dolomite facies (ferroan and non-ferroan dolomite), and post-dolomite calcite (WC) precipitation. Late stage calcite (TC) mostly occluded the pore spaces and is of telogenetic origin. Zebra Dolomite (ZD) and Dolomite Sands (DS) occurred as partially replacive facies of host limestone. Two episodes of mineralisation were observed in the Ranero (Galena-Barite) and El-Moro areas (Sphalerite-Galena);

– isotope geochemistry (O/C stable isotopes and Sr isotopes) revealed that early calcite precipitation (CC-I and CC-II) and dolomitisation (CCD-I) show less depleted $\delta^{18}O$ values, while the subsequent stage dolomite (CCD-II) and calcite (WC) exhibited highly depleted $\delta^{18}O$ values, hence supporting at least two distinct sources of diagenetic fluids. $\delta^{13}C$ values in the dolomites show slight depletion in line with the minor temperature related fractionation effect. Sr isotope confirms that the dolomitising fluids interacted with radiogenic lithologies (sandstones and shales). Depleted $\delta^{18}O$ values (up to – 20.22‰ V-PDB) and high T_h values of the fluid inclusions (up to 200°C; Shah *et al*., 2010) indicate a hot source of dolomitising fluids;

– pervasive dolomitisation resulted from the circulation of basinal fluids, which likely evolved from the shales and clays situated in the deeper part of adjacent basin (Basque trough). NE-SW and NW-SE oriented faults and fractures provided pathways for fluids to dolomitise the early Albian carbonates. Second phase of high temperature, localised dolomitisation may be related to igneous activity and convective flow affecting mainly the Ranero area.

ACKNOWLEDGMENTS

We are indebted to Michael Joachimski (Department of Geology, University of Erlangen), Christophe Renac (Géologie, Université Jean Monnet, Saint-Étienne) for stable isotope analyses. Thanks are also due to Éric Kohler (Geochemistry, IFP Energies nouvelles) for XRD analyses, followed by valuable discussions. Herman Nijs (Geology, K. U. Leuven) and Chantal Perrache (Géologie, Université Jean Monnet, Saint-Étienne) are also acknowledged for thin sections preparation. Lastly, we thank two reviewers (Benoit Vincent and Veerle Vandeginste) for their valuable comments, which lead to a much improved finished product. This work is part of the PhD studies, partially financed by Petrobras and IFP Energies nouvelles.

REFERENCES

Abeger G., Serrano A., Quesada S. (2005) *Petroleum geology of the onshore Cantabrian basin*, in: Martinez del Olmo W. (ed.), Asociación de Geólogos y Geofisicos Españoles del Petróleo AGGEP, pp. 155-162.

Adams J.E., Rhodes M.L. (1960) Dolomitisation by seepage reflux, *AAPG Bull*. **44**, 1912-1920.

Aranburu A., Gómez-Perez I., Fernández-Mendiola P.A., Garcia-Mondéjar J. (1994) Control tectónico sinsedimentario de la serie estratigráfica del sector de Güenes (Albiense, Bizkaia), *Geogaceta* **16**, 82-85.

Badiozamani K. (1973) The dorag dolomitisation model – Application to the middle Ordovician of Wisconsin, *J. Sediment. Petrol*. **43**, 965-984.

Beales F.W., Hardy J.W. (1980) Criteria for recognition of diverse dolomite types with an emphasis on studies of host rocks for Mississippi Valley-type ore deposits, in: Zenger D.H., Dunham J.R., Ethington R.L. (eds), *Concepts and Models of Dolomitisation*, *SEPM Spec. Publ*. **28**, 197-214.

Berger Z., Davies G.R. (1999) The development of linear hydrothermal dolomite (HTD) reservoir facies along wrench or strike-slip fault systems in the western Canada sedimentary basin, *Can. Soc. Petrol. Geol. Reservoir* **26**, 34-38.

Boillot G., Malod J. (1988) The north and north-western Spanish continental margin: a review, *Revista de la Sociedad Geologica de España* **1**, 3-4, 295-316.

Boni M., Parente G., Vivo B.D., Lannace A. (2000) Hydrothermal dolomites in SW Sardinia (Italy): Evidence for a widespread late-Variscan fluid flow event, *Sediment. Geol.* **131**, 181-200.

Bosák P. (1998) The evolution of karst and caves in the Koněprusy region (Bohemion karst, Czech Republic), Part-II Hydrothermal Paleokarst, *Acta Carsologica* XXVII/**2-3**, 41-61.

Braithwaite C.J.R., Rizzi G., Darke G. (2004) The geometry and petrogenesis of dolomite hydrocarbon reservoirs, *Geol. Soc. London Spec. Publ.* **235**, 1-6.

Bustillo M., Fort R., Ordonez S. (1992) Genetic implications of trace-element distributions in carbonate and non-carbonate phases of limestones and dolostones from western Cantabria, Spain, *Chem. Geol.* **97**, 273-283.

Cantrell D., Swart P., Hagerty R. (2004) Genesis and characterization of dolomite, Arab-D reservoir, Ghawar field, Saudi Arabia, *GeoArabia* **9**, 2, 1-26.

Cervato C. (1990) Hydrothermal dolomitisation of Jurassic-Cretaceous limestones in the Alps (Italy): Relation to tectonics and volcanism, *Geology* **18**, 458-461.

Choquette P.W., James N.P. (1988) Introduction, in *Paleokarst*, James N.P., Choquette P.W. (eds), Springer-Verlag, New York, pp. 1-21.

Conliffe J., Azmy K., Gleeson S.A., Lavoie D. (2010) Fluids associated with hydrothermal dolomitisation in St. George Group, western Newfoundland, Canada, *Geofluids* **10**, 422-437.

Davies G.R., Smith L.B. Jr (2006) Structurally controlled hydrothermal dolomite reservoir facies: An overview, *AAPG Bull.* **90**, 11, 1641-1690.

Dickson J.A.D. (1966) Carbonate identification and genesis as revealed by staining, *J. Sediment. Petrol.* **36**, 491-505.

Dorobek S.L., Smith T.M., Whitsitt P.M. (1993) Microfabrics and geochemistry of meteorically altered dolomite in Devonian and Mississipian carbonates, Montana and Idaho, in: Rezak R., Lavoie D.L. (eds), *Carbonate Microfabrics*, Springer-Verlag, New York, pp. 205-225.

Emrich K., Ehhalt D.H., Vogel J.C. (1970) Carbon isotope fractionation during the precipitation of calcium carbonate, *Earth Planet. Sci. Lett.* **8**, 363-371.

Garcia-Mondéjar J. (1985) Carbonate platform-basin transitions in the Soba reef area (Aptian-Albian of western Basque-Cantabrian region northern Spain), in: Mila M.D., Rosell J. (eds), *Sedimentation and Tectonics in the Western Basque-Cantabrian area (northern Spain) during Cretaceous and Tertiary Times*, *6th European Regional Meeting of Sedimentology*, Abstracts book, Int. Assoc. Sedimentol., pp. 172-175.

Garcia-Mondéjar J. (1989) Strike-slip subsidence of the Basque-Cantabrian basin of northern Spain and its relationship to Aptian-Albian opening of Bay of Biscay, in: Tankard A.J., Balkwill H.R. (eds), *Extensional tectonics and stratigraphy of the North Atlantic Margins*, *AAPG Memoir* **46**, 395-409.

Garcia-Mondéjar J. (1996) Plate reconstruction of the Bay of Biscay, *Geology* **24**, 635-638.

Garcia-Mondéjar J., Pujalte V. (1975) Contemporaneous tectonics in the Early Cretaceous of central Santander province, North Spain, *IX^e Congrès International de Sedimentologie*, in: Mangin J.Ph. (ed.), Nice, **4**, pp. 131-137.

Garcia-Mondéjar J., Agirrezabala L.M., Aranburu A., Fernandez-Mendiola P.A., Gomez-Perez I., Lopez-Horgue M., Rosales I. (1996) Aptian-Albian tectonic pattern of the Basque-Cantabrian basin (northern Spain), *Geol. J.* **31**, 13-45.

Garcia-Mondéjar J., Lopez-Horgue M.A., Aranburu A., Fernandez-Mendiola P.A. (2005) Pulsating subsidence during a rift episode: Stratigraphic and tectonic consequences (Aptian-Albian, northern Spain), *Terra Nova* **17**, 517-525.

Gasparrini M. (2003) Large-scale hydrothermal dolomitisation in the southwestern Cantabrian Zone (NW Spain): Causes and controls of the process and origin of the dolomitizing fluids, *PhD Thesis*.

Gasparrini M., Bechstadt T., Boni M. (2006) Massive hydrothermal dolomites in the southwestern Cantabrian Zone (Spain) and their relation to the Late Variscan evolution, *Mar. Petrol. Geol.* **23**, 543-568.

Gibbons W., Moreno M.T. (eds) (2002) *The Geology of Spain*, Geological Society, London.

Giles M.R., de Boer R.B. (1989) Secondary porosity: creation of enhanced porosities in the subsurface from the dissolution of carbonate cements as a result of cooling formation waters, *Mar. Petrol. Geol.* **6**, 261-269.

Graybeal A.L., Heath R.G. (1984) Remobilization of transition metals in surficial pelagic sediments from the eastern Pacific, *Geochim. Cosmochim. Acta* **48**, 965-975.

Gregg J.M., Shelton K.L. (1989) Minor and trace element distributions in the Bonneterre Dolomite (Cambrian), southeast Missouri: Evidence for possible multiple-basin fluid sources and pathways during lead-zinc mineralisation, *Geol. Soc. Am. Bull.* **101**, 221-230.

Grimaud S., Boillot G., Collette B.J., Mauffret A., Miles P.R., Roberts D.B. (1982) Western extension of the Iberian-European plate boundary during the Early Cenozoic (Pyrenean) convergence: a new model, *Mar. Geol.* **45**, 63-77.

Jones B., Robert L.W., Macneil A.J. (2001) Powder X-ray diffraction analysis of homogeneous and heterogeneous sedimentary dolostones, *J. Sediment. Res.* **71**, 790-799.

Land L.S. (1983) The application of stable isotopes to studies of the origin of dolomite and to problems of diagenesis of clastic sediments, in: Arthur M.A., Anderson T.F. (eds), Stable isotopes in Sedimentary Geology, Soc. Econ. Paleont. Miner. Short Course No. 10, 4.1-4.22.

Leach D.L., Sangster D.F., Kelley K.D., Large R.R., Garven G., Allen A.R., Gutzmer J., Walter S. (2005) Sediment-hosted Lead-Zinc deposits: a global perspective, *Economic Geology*, 100th Anniversary Volume, 561-607.

Lopéz-Horgue M., Fernandez-Mendiola P., Iriarte E., Sudrie M., Caline B., Gomez J., Corneyllie H. (2005) Fault - Related Hydrothermal Dolomite Bodies in Early Cretaceous Platform Carbonates Karrantza Area (North Spain): Outcrop Analogue for Dolomite Reservoir Characterization, *10^e Congrès Français de Sédimentologie*, Presqu'île de Giens, France, 7-10 octobre, Abstract.

Lopéz-Horgue M.A., Iriarte E., Schroder S., Fernandez-MendiolaP.A., Caline B., Corneyllie H., Frémont J., Sudrie M., Zerti S. (2010) Structurally controlled hydrothermal dolomites in Albian carbonates of the Ason valley, Basque Cantabrian Basin, Northern Spain, *Mar. Petrol. Geol.* **27**, 1069-1092.

Lopéz-Horgue M.A., Owen H.G., Aranburu A., Fernandez-Mendiola P.A., Garcia-Mondéjar J. (2009) Early late Albian (Cretaceous) of the central region of the Basque-Cantabrian Basin, northern Spain: Biostratigraphy based on ammonites and orbitolinids, *Cretac. Res.* **30**, 385-400.

Lumsden D.N. (1979) Discrepancy between thin section and X-ray estimates of dolomite in limestone, *J. Sediment. Petrol.* **49**, 429-436.

Lumsden D.N., Chimahusky J.S. (1980) Relationship between dolomite nonstoichiometry and carbonate facies parameters, *SEPM Spec. Publ.*, Tulsa, **28**, 123-137.

Machel H.G. (2004) Concepts and models of dolomitisation: A critical reappraisal, *Geol. Soc. London Spec. Publ.* **235**, 7, 63.

Machel H.G., Mountjoy E.W. (1987) General constraints on extensive pervasive dolomitisation – and their application to the Devonian carbonates of western Canada, *Bull. Can. Pet. Geol.* **35**, 143-158.

Malod J.A., Mauffret A. (1990) Iberian plate motions during the Mesozoic, *Tectonophysics* **184**, 261-278.

McArthur J.M., Howarth R.J., Bailey T.R. (2001) Strontium isotope stratigraphy: LOWESS Version 3. Best-fit line to the marine Sr-isotope curve for 0 to 509 Ma and accompanying look-up table for deriving numerical age, *J. Geol.* **109**, 155-169.

Meyers W.J. (1991) Calcite cement stratigraphy, in: Baker C.E., Kopp O.C. (eds), *Luminescence microscopy and spectroscopy: Qualitative and quantitative aspects*, *SEPM short course* **25**, 133-148.

Montadert L., Roberts D.G., de Charpal O., Guennoc P. (1979) Rifting and subsidence of the northern continental margin of the Bay of Biscay, in *Initial reports of the deep sea drilling project*, 48, United States Government Printing office, Washington, pp. 1025-1059.

Moore C.H. (2001) Carbonate Reservoirs: Porosity evolution and diagenesis in a sequence stratigraphic framework, *Development in Sedimentology*, Elsevier Science B.V., Amsterdam.

Nader F.H., Swennen R. (2004) The hydrocarbon potential of Lebanon: New insights from regional correlations and studies of Jurassic dolomitisation, *J. Petrol. Geol.* **27**, 253-275.

Nader F.H., Dumont C., Shah M.M., Garcia D., Swennen R., Daniel J.-M., Lerat O., Doligez B. (2009) From field study to numerical modelling of hydrothermal dolomitisation in Early Cretaceous platform carbonates (Cantabrian mountains, northern Spain), *J. Geochem. Explor.* **101**, 73.

Nader F.H., Lopéz-Horgue M.A., Shah M.M., Dewit J., Garcia D., Swennen R., Iriarte E., Muchez Ph., Caline B. (2011) The Ranero hydrothermal dolomites (Albian, Karrantza valley, northwestern Spain): An outstanding case-study of HTD, *Oil Gas Sci. Technol. - Rev. IFP Energies nouvelles* (in press).

Nader F.H., Swennen R., Ellam R. (2007) Field geometry, petrography and geochemistry of a dolomitisation front (Late Jurassic, central Lebanon), *Sedimentology* **54**, 1093-1119.

Nader F.H., Swennen R., Keppens E. (2008) Calcitization/ dedolomitisation of Jurassic dolostones (Lebanon): results from petrographic and sequential geochemical analyses, *Sedimentology* **55**, 1467-1485.

Nielsen P., Swennen R., Keppens E. (1994) Multiple – step recrystallization within massive ancient dolomite units: an example from the Dinantian of Belgium, *Sedimentology* **41**, 567-584.

Niemann J.C., Read J.F. (1988) Regional cementation from unconformity-recharge aquifer and burial fluids. Mississipian Newman Limestone, Kentucky, *J. Sediment. Petrol.* **58**, 688-705.

Olivet J.L. (1996) La cinématique de la plaque ibérique, *Bulletin des Centres de Recherches Exploration-Production Elf-Aquitaine* **20**, 131-195.

Pujalte V. (1977) Sedimentary succession and paleo-environments within a fault-controlled basin: the "Wealden" of the Santander area, northern Spain, *Sediment. Geol.* **28**, 293-325.

Qing H., Mountjoy E.W. (1989) Multistage dolomitisation in rainbow buildup, Middle Devonian Keg River Formation, Alberta, Canada, *J. Sediment. Petrol.* **59**, 114-126.

Radke B.M., Mathis R.L. (1980) On the formation and occurrence of saddle dolomites, *J. Sediment. Res.* **50**, 4, 1149-1168.

Rat P. (1959) Les pays crétacés Basco-Cantabriques (Espagne), *Thèse*, Publication de l'Universitè de Dijon, 23, 525 p.

Reeder R.J. (1991) An over-view of zoning in carbonate minerals, in: Baker C.E., Kopp O.C. (eds), *Luminescence microscopy and spectroscopy: Qualitative and quantitative aspects*, *SEPM short course* **25**, 77-82.

Ronchi P., Jadoul F., Ceriani A., Di-Giulio A., Scotti P., Ortenzi A., Massara E.P. (2011) Multistage dolomitisation and distribution of dolomitised bodies in Early Jurassic carbonate platforms (Southern Alps, Italy), *Sedimentology* **58**, 532-565.

Rosales I. (1995) La plataforma carbonatada de Castro Urdiales (Aptiense-Albiense, Cantabria), *Thesis Doctoral*, Univ. Pais Vasco, p. 496.

Rosales I., Pérez-Garcia A. (2010) Porosity development, diagenesis and basin modelling of a Lower Cretaceous (Albian) carbonate platform from northern Spain, *Geol. Soc. London Spec. Publ.* **329**, 317-342.

Rosenbaum J., Sheppard S.M. (1986) An isotopic study of siderites, dolomites and ankerites at high temperatures, *Geochim. Cosmochim. Acta* **50**, 1147-1150.

Schärer U., de Perseval P., Polvé M., de Saint Blanquat M. (1999) Formation of the Trimouns talc-chlorite deposit (Pyrenees) from the persistent hydrothermal activity between 112-97 Ma, *Terra Nova* **11**, 1, 30-37.

Shah M.M. (2008) Petrographic, geochemical and petrophysical characteristics of the hydrothermal dolomites (Cretaceous) in the Cantabrian mountains, Ranero area (Spain), *DES report IFP,* No. 60, 532, p. 88.

Shah M.M. (2011) Dolomies hydrothermales dans les carbonates de plateformes (Albien précoce) de la zone de Ranero (Espagne du NW): Distribution, pétrographie, géochimie et genèse, *PhD Thesis*, pp. 1-245, unpublished.

Shah M.M., Nader F.H., Dewit J., Swennen R., Garcia D. (2010) Fault-related hydrothermal dolomites in Cretaceous carbonates (Cantabria, northern Spain): Results of petrographic, geochemical and petrophysical studies, *Bull. Soc. Géol. Fr.* **181**, 4, 391-407.

Sudrie M., Caline B., Lopez-Horgue M.A., Fernandez-Mendolia P.A., Iriarte E. (2006) Fault – related hydrothermal dolomites in Cretaceous platform carbonates from the Karrantza area (north Spain): Outcrop analogues for dolomite reservoir characterization, *7th Middle East Geosciences Conference and Exhibition*, Behrain, Conference Program, CD format.

Swennen R., Dewit J., Fierens E., Muchez Ph., Nader F., Shah M., Hunt D. (2011) Multiple fluid flow dolomitisation events along the Ranero Fault (Pozalagua Quarry, Basque-Cantabrian Basin) explained by episodic earthquake activity, *Sedimentology* (in press).

Swennen, R., Vandeginste, V., Ellam, R. (2003) Genesis of zebra dolomites (Cathedral Formation: Canadian cordillera fold and thrust belt, British Columbia), *J. Geochem. Explor.* **78-79**, 571-577.

Symons D.T., Lewchuk M.T., Kawasaki K., Velasco F., Leach D.L. (2009) The Reocin zinc-lead deposit, Spain: paleomagnetic dating of a late Tertiary ore body, *Miner. Deposita* **44**, 867-880.

Thiébaut J., Debeaux M., Durand-Wackeneheim C., Souquet P., Gourinard Y., Bandet Y., Fondecave-Wallez M.J. (1988) Métamorphisme et halocinèse crétacés dans les évaporites de Betchat le long du Chevauchement Frontal Nord-Pyrénéen (Haute-Garonne et Ariège, France), *C. R. Acad. Sci., Sér. 2, Sci. Terre Planètes* **307**, 1535-1540.

Tompkins L.A., Murray J.R., Groves D.A. (1994) Evaporites: *In situ* source for rhythmically bounded ore in the Cadjebut Mississipi valley type Zn-Pb deposits, western Australia, *Econ. Geol.* **89**, 467-492.

Vandeginste V., Swennen R., Gleeson S.A., Ellam R. (2005) Zebra dolomitisation as a result of focused fluid flow in the rocky mountains fold and thrust belt, Canada, *Sedimentology* **52**, 1067-1095.

Veizer J., Ala D., Azmy K., Bruckschen P., Buhl D., Bruhn F., Carden G.A.F., Diener A., Ebneth S., Godderis Y., Jasper T., Korte C., Pawellek F., Podlaha O., Strauss H. (1999) $^{87}Sr/^{86}Sr$, $\delta^{13}C$ and $\delta^{18}O$ evolution of Phanerozoic seawater, *Chem. Geol.* **161**, 59-88.

Velasco F., Herrero J.M., Yusta I., Alonso J.A., Seebold I., Leach D. (2003) Geology and geochemistry of the Reocin Zinc-Lead deposit, Basque-Cantabrian Basin, Northern Spain, *Econ. Geol.* **98**, 1371-1396.

Vicente-Bravo J.C., Robles S. (1995) Large scale mesotopographic bedforms from the Albian Black Flysch, northern Spain: Characterization, setting and comparison with recent analogues, in: Pickering K.T., Hiscott R.N., Kenyon N.H., Ricci Lucchi F., Smith R.D.A. (eds), *Atlas of Deep Water Environments: Architectural Style in Turbidite Systems*, Chapman and Hall, London, pp. 216-226.

Wachter E., Hayes J.M. (1985) Exchange of oxygen isotopes in carbon-dioxide-phosphoric acid systems, *Chem. Geol.* **52**, 365-374.

Warren J.K. (2000) Dolomite: occurrence, evolution and economically important associations, *Earth-Sci. Rev.* **52**, 1-81.

Wilson E.N., Hardie L.A., Philips O.M. (1990) Dolomitisation front geometry, fluid flow patterns and the origin of massive dolomite: the Triassic Latemar buildup, Northern Italy, *Am. J. Sci.* **290**, 741-796.

Zhao W., Luo P., Chen G., Cao H., Zhang B. (2005) Origin and reservoir rock characteristics of dolostones in the Early Triassic Feixianguan, NE Sichuan Basin, China: significance for future gas exploration, *J. Petrol. Geol.* **28**, 83-100.

Final manuscript received in May 2011
Published online in February 2012